Graphical Abstract

Mesoscopic simulations of inertial drag enhancement and polymer migration in viscoelastic solutions flowing around a confined array of cylinders

David Nieto Simavilla, Marco Ellero

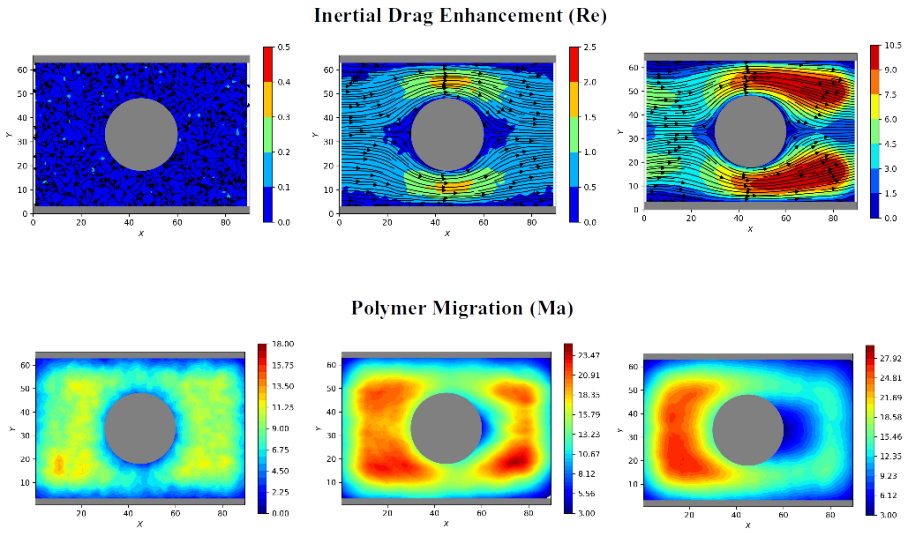

Highlights

Mesoscopic simulations of inertial drag enhancement and polymer migration in viscoelastic solutions flowing around a confined array of cylinders

David Nieto Simavilla, Marco Ellero

- A mesoscopic model fluid combining SDPD particles and FENE springs to mimic viscoelastic behavior is presented.
- The transition from viscous to inertial drag around a confined array of periodically spaced cylinders is investigated with a simple model for inertial and viscous drag.
- Polymeric migration away from the wake of the cylinders is investigated.

Mesoscopic simulations of inertial drag enhancement and polymer migration in viscoelastic solutions flowing around a confined array of cylinders

David Nieto Simavilla[a], Marco Ellero[a,b,c]

[a] *Basque Center for Applied Mathematics (BCAM), Alameda Mazarredo 14, Bilbao, 48400, Vizcaya, Spain*
[b] *IKERBASQUE, Basque Foundation for Science, Calle de Maria Dias de Haro 3, Bilbao, 48013, Vizcaya, Spain*
[c] *Zienkiewicz Centor for Computational Engineering (ZCCE), Swansea University, Bay Campus, Swansea, SA1 8EN, , United Kingdom*

Abstract

We study the flow around a periodic array of cylinders using a mesoscopic viscoelastic fluid that mimics polymeric solutions. We model our fluid employing a novel mesoscopic method based on Smoothed Dissipative Particle Dynamics and FENE springs. We characterize the static and dynamic properties of our model solutions and compare the results with theoretical predictions based on the Zimm model. After rheological characterization of the modeled solutions, we simulate the flow around a confined array of cylinders. The balance between inertia and elasticity in our simulations is studied using a wide range of Reynolds (Re) and Weissenberg (Wi) numbers. We find that increasing the flow rate reduces the drag coefficient on the cylinder up to a critical Re corresponding to a minimum. Thereafter, inertia becomes dominant and we encounter drag enhancement for all the solutions studied, including the Newtonian solvent. With the use of simple model for the viscous and inertial contributions to drag, we conclude that inertial effects are driving the increase in the drag experienced by the cylinder. In our simulations, we also observe migration of polymer chains away from the channel walls and in the wake of the cylinder. We conclude that stress gradients induced by the curvature of streamlines and convection of the depleted layers at the walls as the principal mechanisms driving the migration of chains. We find the extent of the migration correlates well with the viscoelastic Mach number (Ma=$\sqrt{\mathrm{ReWi}}$) suggesting both elastic and inertial effects play a role

in this phenomenon.

Keywords: mesoscopic simulations, viscoelasticity, flow around a cylinder

1. Introduction

In contrast to Newtonian fluids, the viscoelastic properties of polymer solutions result in complex behavior when the polymer chains immersed in the fluids orient and stretch giving rise to additional contributions to the stress. One of the phenomena observed in the flow of polymer solutions is the presence of instabilities that resemble turbulent flow at low Reynolds number (Re) [1]: a balance between inertia and viscous forces. Extensive research has focused on the study of inertia-less flows using theory to predict elasticity-driven chaotic flow structures [2], or experimental observations focused on elastic turbulence at very low Re numbers in contraction flows [3, 4], cross-slot flows [5], flow around a cylinder [6, 7], and flow around arrays of periodically spaced cylinders [8, 9]. The last two geometries are particularly interesting since they constitute a classic example of a mixed flow with strong shear in the gap between the cylinder and the walls and extensional (compression) flow at the stagnation point in the front (wake) of the cylinder [10]. Although some studies have identified flow curvature and large deformation rates as the key conditions for inducing this kind of instabilities [11], Pan *et al.* showed that the flow of polymer solutions becomes unstable at sufficiently high rates no matter the type of flow [12].

In polymeric solutions the elasticity of the fluid is often characterized through the Weissenberg number (Wi): the ratio of the polymer relaxation time and the characteristic time for the experiment. At high Wi the elasticity becomes important whereas at low Wi, Newtonian-like viscous behavior is observed. However, it is often the case that Wi is increased by raising the flow rate, and therefore, it also results in an increase of the Re number. At higher Re numbers, inertial effects become also important and it has been suggested that the relevant dimensionless quantity is the elasticity number El=Wi/Re [13]: a ratio between the polymer relaxation time and the characteristic viscous time. In these studies, the traditional chaotic motion observed in turbulence is replaced by a different form of disordered flows termed as Elasto-Inertial Turbulence (EIT) [14, 15, 16]. In the elasto-inertial regime, Nolan and coworkers have investigated the flow around a single cylinder in a microfluidics channel of aqueous solutions of polyacrylamide by particle im-

age velocimetry [17]. This work shows how vortex separation is suppressed in viscoelastic fluids and a long wake downstream of the cylinder takes place due to elasticity and the longer relaxation time of polymers. In spite of the extensive research investigating polymer induced instabilities at low Reynolds numbers, numerical studies exploring elastic and elasto-inertial turbulence at moderate Reynolds numbers is limited [18].

Another interesting phenomena observed in dilute polymeric solutions is the migration or separation of chains induced by flow. This phenomena results in a non-homogeneous polymer concentration in the fluid domain. Polymer migration has been proposed as a driving mechanism for DNA separation using a spinning cone geometry [19]. This mechanism for DNA separation via migration was confirmed using a similar geometry by MacDonald and Muller [20]. Recently, the conformation of individual DNA molecules in flow through an array of cylinders has been investigated experimentally [21]. This study found dead zones – areas where a depletion of DNA molecules is observed – that form upstream of cylinders at a viscoelastic Mach number $\mathrm{Ma}=\sqrt{\mathrm{ReWi}} \sim 1$. The formation of dead zones is explained by strong conformational fluctuations related to the stretching and recoiling of molecules. Shi et al. [22] examined upstream and downstream instabilities that occur for highly confined and bounded viscoelastic flows around a cylinder using Boger fluids. Their study reports the onset of downstream instabilities at $\mathrm{Ma}=1$ that are caused by a disturbance of the base flow by traveling elastic waves. Upstream instability, which depends on both the geometry and the fluid, was only observed at $\mathrm{Ma}\sim 10$ and resulted in a significantly increased flow resistance. A linear array of cylinders was later investigated at moderate Ma numbers [23]. In this geometry, instabilities developed downstream of the cylinders and grew upstream until – at sufficiently high Ma – a vortex was created.

An exhaustive analysis of the possible mechanisms leading to polymer migration in confined geometries was proposed by Jiang *et al.* [24]:

1. Wall exclusion from layers with a size comparable to the polymer gyration radius R_g. Under this mechanism the depletion layer will be larger for longer and flexible polymers.
2. Sieving of chains due to narrow section of the geometry limiting the passing of polymer molecules. This effect is most important at $\mathrm{Wi}< 1$ when the chains remain unstretched.
3. Migration due to hydrodynamic interactions with the wall. For $\mathrm{Wi}< 10$

this effect has been shown to be small and very slow at driving polymer migration [24]. However, it has been shown that long contraction regions can results in significant migration due to this mechanism [25], with the migration mechanism scaling as Wi^2.

4. Streamline-curvature-induced (SCI) migration: Polymers traveling along curved streamlines migrate towards the center of curvature due to the induced stress gradient. At Wi$>$ 1, dominant curvature induced migration has been confirmed experimentally [19, 20] and the rate of migration has been found to be proportional to Wi^2.
5. Depletion-convection-induced (DCI) migration. Depleted layers (i.e., created near the wall by Mechanism 1) grow through convective transport driven by a diffusion imbalance. This mechanism becomes dominant at large Péclet (Pe): when advective transport overcomes mass diffusion.

The effectiveness of each mechanism needs to be evaluated depending on the geometry, the equilibrium polymer size R_g and the dimensionless numbers Re, Pe and Wi [24]. All mechanisms can be relevant in confined geometries (i.e., when R_g and geometry size are comparable). SCI has been shown to govern polymer migration towards the center of curvature in Taylor-vortex flow [26], Taylor-Couette flow [27], and eccentric Taylor-Couette flow [28]. In all these studies SCI is the most relevant mechanism once moderate Wi numbers are reached. The specific Wi threshold for migration seems to be dependent on the gradient number Gd (a measure of confinement) and the ratio of the Pe and Wi numbers characterizing the flow constriction.

In this study, we present a particle-based mesoscopic model for dilute polymer solutions to study flow around a periodic array of confined cylinders. Fluid particles are modeled using the Smoothed Dissipative Particle Dynamics (SDPD) method. To introduce viscoelasticity, we form chains linking some of the particles using FENE springs. We perform flow simulation over a wide range of Reynolds and Weissenberg numbers by manipulating the flow rate and the polymer relaxation time. We model three different chain lengths (N=25, 50 and 100 particles) to obtain a wide dynamic response and access low-to-moderate regimes in the Re and Wi numbers. First, we present a detailed characterization of the physical parameters of our model including polymer size and diffusion coefficients. We use single chain stretching and relaxation to determine the polymeric characteristic relaxation time. We subject our model to Reverse Poiseuille Flow to characterize the shear rheology

of the model solutions. Our solutions mimic a cross model for the viscosity as a function of the shear rate: a shear thinning transition between plateaus. Finally, we study the flow through a periodic array of confined cylinders. We introduce a simple model to analyze the viscous and inertial contributions to the drag experienced by the cylinders as a function of the characteristic dimensionless numbers. We analyze the migration of chains in our confined geometry and evaluate the primary mechanisms leading to migration. We link the extend of migration with the inertial (Re) and elastic (Wi) effects and find good correlation between the magnitude of the migration and the corresponding viscoelastic Mach number (Ma).

2. Simulation methods

2.1. Smoothed Dissipative Particle Dynamics (SDPD)

In contrast to traditional DPD or SPH methods, SDPD incorporates fluctuations in a particle-based Lagrangian discretization of Navier-Stokes (N-S) equations [29]. The method presents an important key difference: SDPD is compliant with the GENERIC formalism. As a result, the method respects the first and second law of thermodynamics and the incorporation of thermal fluctuations leads to the correct equilibrium probability distribution given by Einstein's formula [29]. In addition, SDPD model parameters are directly connected to the physical parameters (density, speed of sound and viscosity) of the simulated system making it possible to give a physical interpretation of the simulation results[30].

In SDPD, the fluctuating N-S equations are discretized to a set of stochastic differential equations for the position $\boldsymbol{r}_i$, velocity $\boldsymbol{v}_i$ and entropy S_i of a set of discrete N_{SDPD} particles[29]. In the present manuscript, we consider only the mass and momentum balances since we are working with isothermal flows. The evolution of the particles position and momentum are given by

$$\frac{d\boldsymbol{r}_i}{dt} = \boldsymbol{v}_i \tag{1}$$

$$m\frac{d\boldsymbol{v}_i}{dt} = \boldsymbol{F}_i \tag{2}$$

where $\boldsymbol{F}_i$ is the force acting on each SDPD particle that can be split on its conservative (c), dissipative (d), random (r) and external (e) contributions (i.e., $\boldsymbol{F}_i = \sum_j \left(\boldsymbol{F}_{ij}^{\mathrm{c}} + \boldsymbol{F}_{ij}^{\mathrm{d}} + \boldsymbol{F}_{ij}^{\mathrm{r}}\right) + \boldsymbol{F}_i^{\mathrm{e}}$). Note that all force contributions with

the exception of the external the result of the sum of pair interaction in between fluid particles. Each contribution is given by

$$\boldsymbol{F}_{ij}^{\mathrm{c}} = -\sum_j \left[\frac{p_i}{d_i^2} + \frac{p_j}{d_j^2}\right] \tilde{F}_{ij}\boldsymbol{r}_{ij} \tag{3}$$

$$\boldsymbol{F}_{ij}^{\mathrm{d}} = -\sum_j \left[a_{ij}\boldsymbol{v}_{ij} + b_{ij}(\boldsymbol{v}_{ij}\cdot\boldsymbol{e}_{ij})\boldsymbol{e}_{ij}\right] \frac{\tilde{F}_{ij}}{d_i d_j} \tag{4}$$

$$\boldsymbol{F}_{ij}^{\mathrm{r}} = \sum_j \left[A_{ij} d\overline{\boldsymbol{W}}_{ij} + \frac{B_{ij}}{3}\mathrm{tr}(d\boldsymbol{W}_{ij})\right] \cdot \boldsymbol{e}_{ij} \tag{5}$$

where $\boldsymbol{r}_{ij} = \boldsymbol{r}_i - \boldsymbol{r}_j$, $\boldsymbol{v}_{ij} = \boldsymbol{v}_i - \boldsymbol{v}_j$, $\boldsymbol{e}_{ij} = \boldsymbol{r}_{ij}/r_{ij}$ and $r_{ij} = |\boldsymbol{r}_i - \boldsymbol{r}_j|$. The particle density is calculated as $d_i = 1/\mathcal{V}_i = \sum_j W_{ij}$, where $W_{ij} = W(r_{ij}, r_{\mathrm{c}})$ is a normalized kernel function of finite support r_{c}. Following previous work using SDPD particles we have adopted Lucy kernel [31]:

$$W(r, r_{\mathrm{c}}) = \begin{cases} \frac{105}{16\pi r_{\mathrm{c}}^3}\left(1 + 3\frac{r}{r_{\mathrm{c}}}\right)\left(1 - \frac{r}{r_{\mathrm{c}}}\right)^3 & \text{if } r/r_{\mathrm{c}} \leq 1 \\ 0 & \text{if } r/r_{\mathrm{c}} > 1 \end{cases} \tag{6}$$

To facilitate the discretization of the N-S equations, it is useful to define the function $\tilde{F}_{ij} = -W'(r_{ij}, r_{\mathrm{c}})/r_{ij}$, where the prime denotes the derivative with respect r_{ij}. In Eq. (3) above the pressure p_i is given by Tait's equation of state [32]:

$$p_i = p_0\left[\left(\frac{\rho_i}{\rho_0}\right)^{\gamma} - 1 + \tilde{p}_{\mathrm{b}}\right] \tag{7}$$

where p_0, ρ_0 and γ parameters are chosen to minimize density variations ($< 5\%$) by choosing a sufficiently large speed of sound $c_{\mathrm{s}} = \sqrt{p_0\gamma/\rho_0}$. A background pressure $\tilde{p}_{\mathrm{b}} = 0.7$ ensures positive pressure across the domain for the range of deformation rates studied, which provides numerical stability [31]. For all our simulations with choose a time step $\Delta t = 0.003$ given by the shorter time scale in the Courant-Friedrich-Lewy condition $\delta t_c = dx/32c_{\mathrm{s}}$ and $\delta t_\eta = dx^2/16\eta$ [33, 34]. In Eq. (4), $a_{ij} = 5\eta/3 - \zeta$ and $b_{ij} = 5(\zeta + \eta/3)$ are friction coefficients given by the shear η and bulk ζ viscosities. In Eq. (5), the amplitudes of the thermal noises A_{ij} and B_{ij} are chosen to satisfy

the Fluctuation-Dissipation Theorem:

$$A_{ij} = \left[4k_{\mathrm{B}} T a_{ij} \frac{\tilde{F}_{ij}}{d_i d_j} \right]^{1/2} \tag{8}$$

$$B_{ij} = \left[4k_{\mathrm{B}} T \left(b_{ij} - a_{ij}/3 \right) \frac{\tilde{F}_{ij}}{d_i d_j} \right]^{1/2} \tag{9}$$

For the random contribution to the force in Eq. (5), $d\boldsymbol{W}_{ij}$ is a matrix of independent increments of the Wiener process and $d\overline{\boldsymbol{W}}_{ij}$ its traceless symmetric part. For additional details on the SDPD model and its implementation the reader is referred to [29, 30].

2.2. Polymer chains

To introduce viscoelasticity into our model, we form polymer chains by linking solvent-like particles with Finite Extensible Non-linear Elastic (FENE) springs [35]:

$$\boldsymbol{F}_{ij}^{\mathrm{FENE}} = \frac{H \boldsymbol{r}_{ij}}{1 - (r_{ij}/r_{\max})^2} \tag{10}$$

where $H = bk_B T / r_{\max}^2$ is the spring elastic constant, $\boldsymbol{r}_{ij}$ is vector connecting to consecutive particles forming a bond in the polymer chain, $r_{\max} = 1.4dx$ is the limit value for the extensibility of the spring and b a scale factor balancing elastic and thermal forces acting on the particles. Note that polymer topology is preserved thanks to the choice of a small maximum bond length relative to the average inter-particle distance $dx = 1$ (i.e., bond crossing is prevented). Under these conditions the system quickly equilibrates to a bond length $l \sim 0.6dx$ which is roughly 40% of the limit extensibility. The equilibrium value of l is not strongly affected by the flow conditions in the study. This method for generating chains of SDPD particles have been shown to reproduce the right scaling for static properties and diffusion coefficient of single polymer chains [36]. For solutions constructed in this way with N_{p} polymer chains of N particles each we define the effective polymer concentration as $w = N_{\mathrm{p}} N / N_{\mathrm{SDPD}}$ (i.e., the number of particles connected by FENE springs divided by the total number of particles in the system N_{SDPD}). A summary of the parameters for the SDPD particles and spring constants in the simulated solutions is included in Table 1.

Table 1: Polymer solutions model parameters. A first group gives the SDPD particle parameters. The second group includes the two FENE spring constants. The third group summarizes the dimensionless parameter space in this study.

Parameter	Description	Value
dx	average inter-particle distance	1.0
ρ	density	1.0
m	particle mass	1.0
η_{s}	solvent viscosity	5.0
c_{s}	speed of sound	10
$\tilde{p}_{\mathrm{b}}$	background pressure	0.7
h	smoothing length	$3dx$
$k_{\mathrm{B}}T$	thermal energy	1.0
b	FENE-P spring constant	1000
$r_{\max}$	max. extensibility radius	$1.4dx$
$\mathrm{Re} = VR_{\mathrm{cyl}}/\nu$	Reynolds number	0.2 – 20
$\mathrm{Wi} = V\tau_{\mathrm{p}}/R_{\mathrm{cyl}}$	Weissenberg number	0.2 – 350
$\mathrm{Sc} = \nu/D$	Schmidt number	~ 1400
$\mathrm{EI} = \mathrm{Wi}/\mathrm{Re}$	Elasticity Index	0.3 – 27
$\mathrm{Ma} = \sqrt{\mathrm{ReWi}}$	Viscoelastic Mach number	0.2 – 60

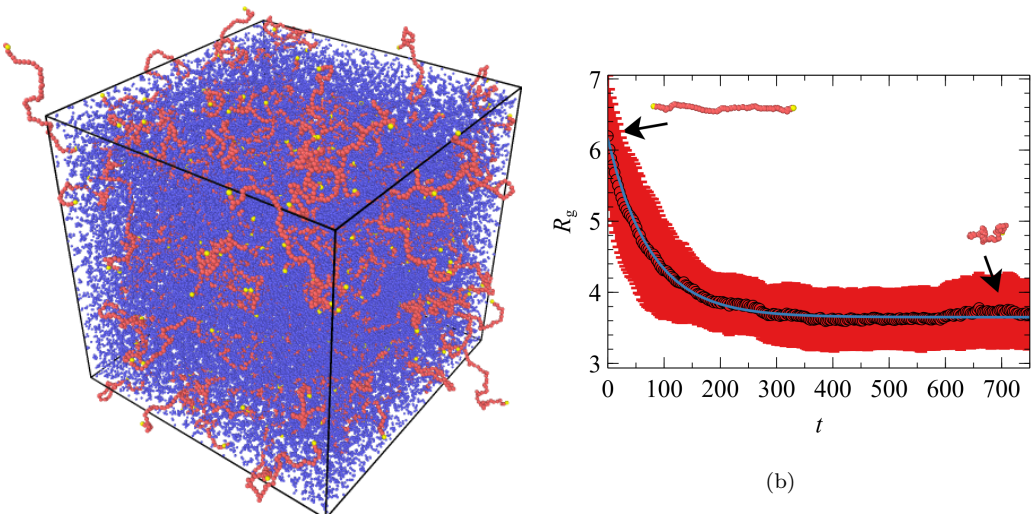

(a) (b)

Figure 1: (a) Initial random configuration for the $30dx \times 30dx \times 30dx$ system with chains N=50 and polymer concentration of w=0.1.(b) Relaxation of a stretched chain (N=50 and w=0.1) averaged over five independent simulations. The solid line represents a fit to a single exponential decay with polymeric relaxation time $\tau_p = 76.6 \pm 10.1$. The position of representative examples of a fully stretched and a coiled equilibrium configuration are indicated by the black arrows.

2.3. Static properties and polymeric relaxation times

To characterize the SDPD model fluid a number of measurements in a system of $30 \times 30 \times 30$ particles in the absence of flow is performed. Initial configurations are generated through random sampling using a Gaussian cumulative distribution function for the position of the particles. Chains are grown sequentially through a self-avoiding random walk [37] that is constrained to the structural parameters in Table 1. An example of a random initial configuration for chains N=50 and polymer concentration w=0.1 is shown in Figure 1a. Using this approach avoided the large simulation times needed to equilibrate initial configurations generated over a regular lattice that limited simulation to relatively short chains (N$\leq$ 25) [36].

First, the solvent diffusion coefficient of a system with no chains is determined from the ensemble average of the mean-squared displacement (MSD) as a function of time:

$$\text{MSD} = 6Dt \tag{11}$$

From the slope of the data in the inset to Figure 2, we find $D = 0.0072$.

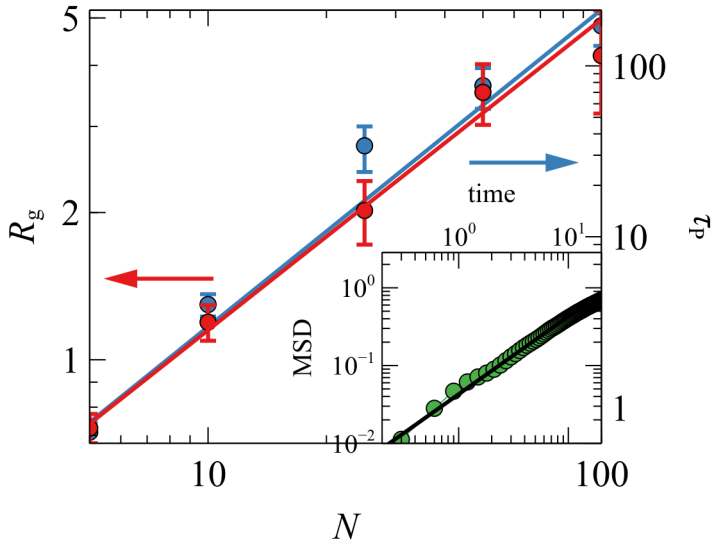

Figure 2: Left axis: Equilibrium gyration radius (red circles) as a function of the chain length N. The red solid line is a power law $R_g \propto N^\nu$ with exponent $\nu = 0.63$. Right axis: polymer relaxation time (blue) as a function of the chain length N. The blue solid line is a power law $\tau_p \propto N^{3\nu}$ with $\nu = 0.62$. The inset shows the mean-squared displacement (MSD) for pure solvent. The solid line shows MSD$= 0.043t$.

Using Stokes-Einstein relation, we can estimate the hydrodynamic radius for each particle in a chain as $r_h = k_B T/6D\pi\eta = 1.48$. This result is consistent with the SDPD particles' cutoff radius $r_c = h = 3dx = 3.0$. In addition, we find a Schmidt number Sc$= \nu/D \sim 1400$, which ensures that momentum diffusion is much faster than mass diffusion as expected for real fluids [38]. The resulting high Sc values are feature of the SDPD method, which has an arbitrary viscosity as a model input and therefore allows direct control over the Sc number [39].

Next, we consider systems with a small concentration of particles $w = 0.1$. By tracking the ensemble average of the gyration radius of all the chains in the system we determine its equilibrium value in 100,000 time steps. Figure 2 (left axis) shows a power law relationship $R_g \propto N^\nu$ between the gyration radius as a function of the number of particles per chain N. The black solid line indicates an exponent $\nu = 0.63 \pm 0.05$, which is about 7% above the asymptotic value for a self-avoiding random walk $\nu = 0.588$ [40]. Finally, we study the relaxation dynamics of individual chains. By pulling at both ends of a chain using forces $F = \pm 20$, we increase the radius of gyration of the chain

to roughly twice its equilibrium value. Once steady state has been reached, we cease the force separating both ends and track the time that the radius of gyration takes to relax back to its equilibrium value. The averaged relaxation dynamics of five independent runs are then fitted using a single exponential decay (See Figure 1b). A similar approach has been used experimentally to establish relaxation dynamics of single polymer chains [41]. Figure 2 (right axis) shows a power law relation between the polymer's relaxation time τ_{p} and the chain length N. Using the Zimm model ($\tau_{\mathrm{p}} \propto N^{3\nu}$), we find $\nu = 0.62 \pm 0.06$, which is in good agreement with the analysis of the radius of gyration. Agreement with the Zimm model indicates a full description of the hydrodynamic interaction between particles in a chain. In contrast, the Rouse model ($\tau_{\mathrm{p}} \propto N^{2\nu+1}$), which does not account for HI between particles in a chain results in a much lower ν, inconsistent with the dependence of the gyration radius on N, and previous work on similar polymer solutions including theoretical [42] and simulation studies modeling mesoscopic fluids [43, 36].

2.4. Rheometric flow measurements

We calculate the shear viscosity according to its definition $\eta = \tau_{xy}/\dot{\gamma}$ where τ_{xy} is the shear stress and $\dot{\gamma}$ the shear rate. To determine the stress, we followed the Irving-Kirkwood-like methodology proposed by Thompson *et al.*[44, 45] to estimate the stress-per-atom (or in our case per particle) in MD simulations using LAMMPS [46]. This method accounts for all the interactions between particles to provide a measure of the stress tensor of a particle i:

$$S^i_{\alpha\beta} = -m v^i_\alpha v^i_\beta - \mathcal{W}^i_{\alpha\beta} \tag{12}$$

where α and β take the values x, y and z. The first term in Eq. 12 corresponds to the kinetic energy contribution for each particle. The second term $\mathcal{W}_{\alpha\beta}$ results from the virial contribution due to particle interactions, which in our model are given by SDPD hydrodynamic and FENE bond interactions computed as

$$\begin{aligned} \mathcal{W}^i_{\alpha\beta} = & \frac{1}{2}\sum_{n=1}^{N_{\mathrm{k}}}(r_{i\alpha}F^{\mathrm{pair}}_{i\beta} + r_{n\alpha}F^{\mathrm{pair}}_{n\beta}) \\ & + \frac{1}{2}\sum_{n=1}^{N_{\mathrm{b}}}(r_{i\alpha}F^{\mathrm{bond}}_{i\beta} + r_{n\alpha}F^{\mathrm{bond}}_{n\beta}) \end{aligned} \tag{13}$$

In Eq. (13), the first sum accounts for each pair interaction with particle positions $\boldsymbol{r}_i$ and $\boldsymbol{r}_n$. The forces $\boldsymbol{F}_i^{\text{pair}}$ and $\boldsymbol{F}_n^{\text{pair}}$ are resulting from the pairwise interaction with N_{k} particle neighbours in the kernel support. The second sum includes the bond interactions $\boldsymbol{F}_i^{\text{bond}}$ and $\boldsymbol{F}_n^{\text{bond}}$ through N_{b} bonds. Note that in our model $N_{\text{b}} = 0$ for solvent particles and, since we work with linear polymer chains, $N_{\text{b}} = 1$ (chain ends) or $N_{\text{b}} = 2$ (backbone particles).

2.5. Reverse Poiseuille Flow (RPF)

We simulate two parallel Poiseuille flows in opposing directions driven by uniform body forces [47]. This method has the singular advantage of avoiding the need of fixed walls, where boundary conditions like no slip need to be imposed [48]. The flow is simply imposed by dividing the simulation domain in two halves and applying a uniform external force in the x-direction $\boldsymbol{F}^{\text{e}} = (F_x^{\text{e}}, 0, 0)$. In the first half of the domain $F_x^{\text{e}} = g$ and in the second half $F_x^{\text{e}} = -g$. In this way, the shear stress imposed in the domain is:

$$\tau_{xy} = \begin{cases} gn(L_y/4 - y) & \text{if } y \leq L_y/2, \\ gn(y - 3L_y/4) & \text{if } y > L_y/2. \end{cases} \tag{14}$$

where n is the number density. Note that the stress in Eq. (14) is dependent on the system length, the imposed force and the number density, but most significantly independent of the solvent viscosity. As a result, the same stress profile is common to all solutions, included the pure solvent with no chains. This presents the opportunity of checking the flow dynamics (as shown in Figure 3a) by comparing it to Eq. (14) with the computed stress.

In our simulations, we follow a start-up protocol where the driving force is turn on suddenly after the thermalization of the system. Thereafter, we track the stress, the velocity profile and the conformation tensor of the chains in the system to establish when steady state is reached. For the analysis of the viscosity, we consider only steady-state flow conditions. To provide a stress measurement that is macroscopically relevant, the local per particle stress is averaged over space dividing the domain in 100 bins or slabs over the y-direction with roughly $N_{\text{bin}} \sim 400$ particles/bin. The stress profiles presented in Figure (3a) are the result of further averaging the stress for each bin in time (i.e., an averages of every $N_{\text{t}} = 1000$ time steps for each bin is given with a timestep $\Delta t = 0.003$):

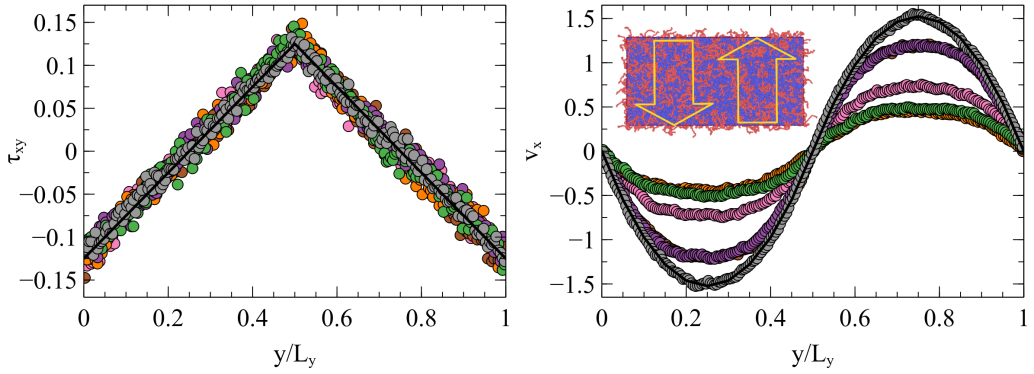

(a) (b)

Figure 3: (a) Imposed shear stress for reverse Poiseuille flow τ_{xy} as a function of the y-coordinate. Points correspond to the stress measured in simulations with different chains lengths and concentrations: solvent (green), $N = 100$ and $w = 1.0$ (green), $N = 50$ and $w = 1.0$ (orange),$N = 100$ and $w = 0.5$ (purple), $N = 50$ and $w = 0.5$ (brown), and $N = 50$ and $w = 0.75$ (pink). The black solid line corresponds to Eq. (14) for $g = 0.005$.(b) Velocity profiles for the same polymer solutions in (a). The inset sketch shows a xy-plane view the $N = 25$ and $w = 0.5$ system, with the arrows showing the direction of flow, solvent particles in blue and polymer (or bonded) particles in pink.

$$\boldsymbol{\tau}(\boldsymbol{x}, t) = \frac{1}{N_{\mathrm{t}} N_{\mathrm{bin}}} \sum_{n=1}^{N_{\mathrm{t}}} \sum_{m=1}^{N_{\mathrm{bin}}} S_{ij} \tag{15}$$

In Figure 3, we show the stress and corresponding velocity profiles for systems of $N = 100$ and $N = 50$ chains at a number of concentrations. In Figure 3a, we show for all the systems the calculated stress corresponds with the theoretical profile given by Eq. (14). For power law fluids (i.e., $\eta = \kappa \dot{\gamma}^p$) an analytical expression can be found for the velocity [47] that is characterized by a flattening of the parabolic profile given for the Poiseuille flow for Newtonian fluids (See Figure 3b). However, the rheological response of our model fluids is more complex than the observed for power law fluids. For example, we will observe a plateau at high and low shear rates connected by a power-law-like response at intermediate Wi. In Figure 3b we also include the parabolic velocity profile that is expected for the pure solvent:

$$V_x(y) = V_{\max} \left[1 - \left(\frac{y}{L_y/4} \right)^2 \right], \tag{16}$$

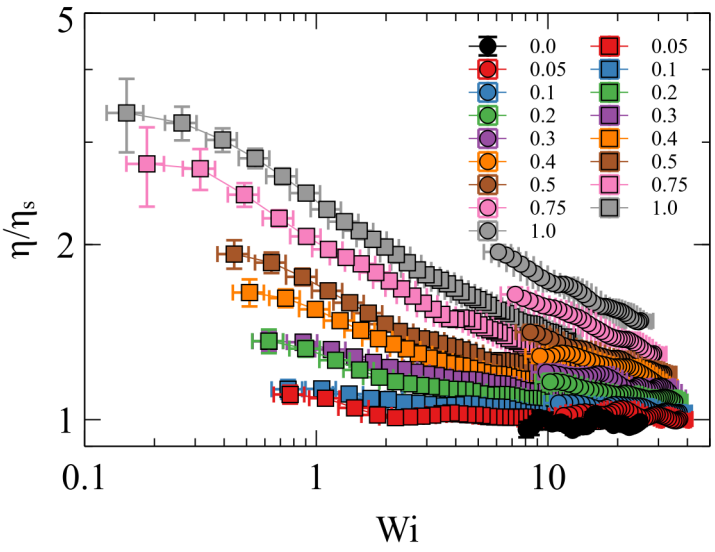

Figure 4: Shear viscosity of solutions as a function of the Weissenberg number for different polymer concentration (indicated by the legend). Viscosity has been normalized by the solvent viscosity η_s. Solutions of chains $N = 25$ ($N = 50$) are represented by squares (circles).

where the peak velocity is given by $V_{\max} = gnL_y^2/32\eta$. As a result of the increased viscosity due to the polymeric stress, the velocity profile of solutions ($w > 0$) peak at lower values. The flattening of the velocity profile in the regions of lower shear rate is a direct result of shear thinning behavior of the solution. These departures from the parabolic velocity profile have been treated in detail in a recent study using the SDPD method [36] using an slightly different parameter space (Sc=770). From the velocity profiles in Figure 3b, we can extract the shear rate profile as $\dot{\gamma} = \partial v_x/\partial y$. To that end, we numerically differentiate the velocity profiles and thereafter apply a Savitzky-Golay filter [49, 50] following the same method described by Baker *et al.* in a similar fluid using DPD particles [48]. Then we use the definition of shear viscosity to compute its values as a function of the shear rate (i.e., $\eta = \tau_{xy}/\dot{\gamma}$), where we take the imposed stress profile to reduce uncertainty.

Figure 4 presents the viscosity as a function of the Weissenberg number for polymer solutions of $N = 25$ and $N = 50$ with concentration ranging between $w = 0.0$ (solvent) and $w = 1.0$. The zero shear viscosity plateau is not unequivocally observed for either system, with the exception of the higher concentrations $w = 0.75$ and $w = 1.0$ for N=25, where a trend towards a

plateau can be noticed. The results presented for the flow around a train of cylinders in the following sections correspond to a concentration $w = 0.5$ (brown symbols in Figure 4). For this specific concentration and for N=25, we can estimate a zero shear viscosity that is roughly twice the solvent viscosity. To calculate Wi, we have used the polymer relaxation time from single chain stretching experiments in Figure 2 with $\tau_{\mathrm{p}}(N = 25) = 34.1 \pm 6$, $\tau_{\mathrm{p}}(N = 50) = 76.6 \pm 10.1$ and $\tau_{\mathrm{p}}(N = 100) = 171 \pm 20.3$.

2.6. Flow around an array of confined cylinders

Figure 5 shows a schematic of the simulated mesoscopic domain ($90 \times 66 \times 20$) for the flow around an array of confined cylinders. The walls and the cylinder are formed by fix particles regularly spaced at a distance $dx = 1$, where no penetration of solvent or polymer particles is allowed. The distance in between the walls is $H = 60dx$, each wall thickness is $3dx$ and the cylinder radius is $R_{\mathrm{cyl}} = 15dx$. Using these dimensions the cylinder covers half of the channel width and the distance between the center of consecutive cylinders, due to the periodicity of the boundaries, is $6R_{\mathrm{cyl}}$ as in a previous studies of viscoelastic flow around an array of cylinders [51, 52, 53]. The key differentiation with these studies is that viscoelasticity was previously modeled by introducing a viscoelastic constitutive equation for the stress (i.e., using Oldroyd-B model [54] for the polymeric stress and the evolution of the conformation tensor as a property the fluid particles). Here, we present a bottom-up mesoscopic model to introduce viscoelasticity using a force based approach. The boundaries are fixed in the y-direction and periodic in the x- and z-directions. Flow is induced by applying an homogeneous force though the fluid domain. To ensure no negative pressure in the domain, the background pressure is set to $\tilde{p}_{\mathrm{b}} = 0.7$ in Eq. (7). This value is selected by progressively increasing $\tilde{p}_{\mathrm{b}}$ while monitoring the pressure in a square region $(5dx) \times L_y \times (5dx)$ in the wake of cylinder for the fastest flow scenarios in the study.

For the calculation of the the Reynolds and Weissenberg numbers, we have considered the average of the velocity field $\bar{v}$ in the outlet region with a width R_{cyl}.

$$\mathrm{Re} = \frac{\rho \bar{v} R_{\mathrm{cyl}}}{\eta_{\mathrm{s}}} \qquad\qquad \mathrm{Wi} = \frac{\bar{\mathrm{v}}}{\mathrm{R_{cyl}}} \tau_{\mathrm{p}} \tag{17}$$

Both of these dimensionless numbers are controlled through the imposed flow rate. For a fix flow rate the ratio between the two (El=Wi/Re) is fixed. Our

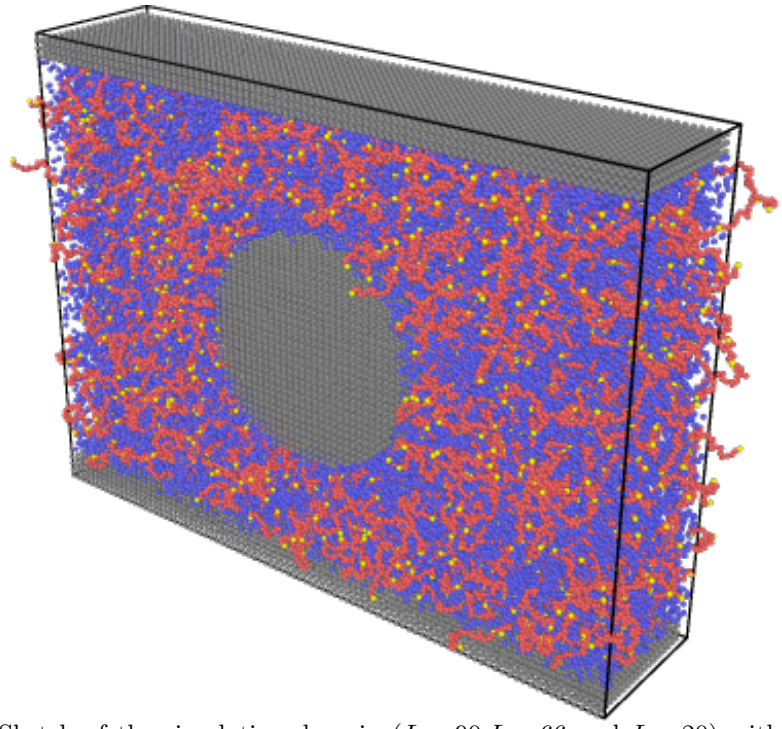

Figure 5: Sketch of the simulation domain (L_x=90,L_y=66 and L_z=20) with a centered cylinder of $R_{\mathrm{cyl}} = 15$. Wall and cylinder particles are fixed and colored in grey, solvent particles are represented in blue, backbone chain particles are colored pink and chain ends are colored in yellow.

simulations cover a wide range in Re (Wi) space and include start-up and cessation of flow but for the current study we focus on the steady-state flow around the periodic array of cylinders. The space for the dimensionless parameters in our simulations is far from the very low Re regime for elastic wave instabilities between obstacles [55]. However, at moderate Re numbers Varshney *et al.* [56] highlight importance of inertia on the stability of viscoelastic flow in a wide range of Wi, Re and their ratio EI=Wi/Re. For high elasticity fluids a complete re-laminarization is found for Re order unity - in contrast to well known drag reduction in turbulent flow. This effect can be explained by finite polymer extensibility and suppression of vorticity at high Wi. In our results however, we observe laminar flow in all simulations including the solvent system in the absence of polymer chains.

3. Results and Discussion

3.1. Inertial drag enhancement

By measuring the drag force F_{D} experienced by the cylinder, we are able to compute the drag coefficient

$$C_{\mathrm{D}} = \frac{F_{\mathrm{D}}}{R_{\mathrm{cyl}}\bar{v}\eta_s} \tag{18}$$

Figure 6 shows C_{D} as a function of the Wi number. We show the drag coefficient for solutions of model polymers with N=25, 50 and 100 particles per chain at a concentration w=0.5. We find drag increase at different Wi numbers depending on the chain length. Our results show an initial drag reduction that can be explained by the decrease in shear viscosity with increasing shear rate (i.e., shear thinning) as the flow driving force is increased [57]. All three systems show a minimum, and thereafter a sharp increase in the drag coefficient. A direct numerical simulation study of flow around a cylinder in 3D of an Oldroyd B fluid has shown laminar flow at moderate Re number in the presence of elastic effects [18]. In that study, for Re$<$ 100 only drag enhancement is found and for larger Re a drag reduction regime precedes the elastic drag enhancement. A second drag reduction regime is expected at much higher Re.

To explain the lack of correlation between the transition to drag enhancement that we observe in Figure 6 and Wi (i.e., the onset of drag enhancement seems to be independent of the elasticity in the solutions), we look at two

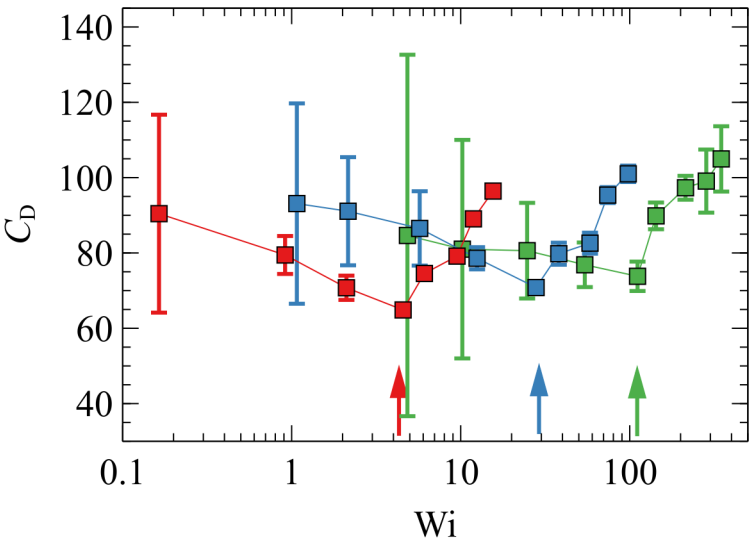

Figure 6: Drag coefficient C_D as a function of the Weissenberg number for system with a polymer concentration $w = 0.5$ and chain lengths of $N = 25$ (red), $N = 50$ (blue) and $N = 100$ (green). The colored arrows represent the onset of drag enhancement in the different systems.

contributions to the drag coefficient: viscous and inertial. For this analysis, we look at the force required to flow through viscous media and the force required to displace the fluid along the path of a moving cylinder [58]:

$$F_V = CR_{cyl}^2 \eta \dot{\gamma} \tag{19}$$

$$F_I = C' \rho R_{cyl}^4 \dot{\gamma}^2 \tag{20}$$

These are often referred to as viscous and inertial drag forces. Here, we remark that the most conventional definition of the drag force is given by (20) or equivalently $F_{drag} \propto \rho \bar{v}^2 A$, where A is a characteristic area. This is often the choice for the characterization of the drag at high Re and results on the drag being inversely proportional to Re in the laminar regime. Instead, we have chosen the viscous drag definition given by (19) as our study is limited to a range from low (but finite) to moderate Re. Note that using this definition C_D is expected to be constant in the low Re regime and that $\mathrm{Re} \propto F_I/F_V$. Now, we can consider the drag force given by adding both

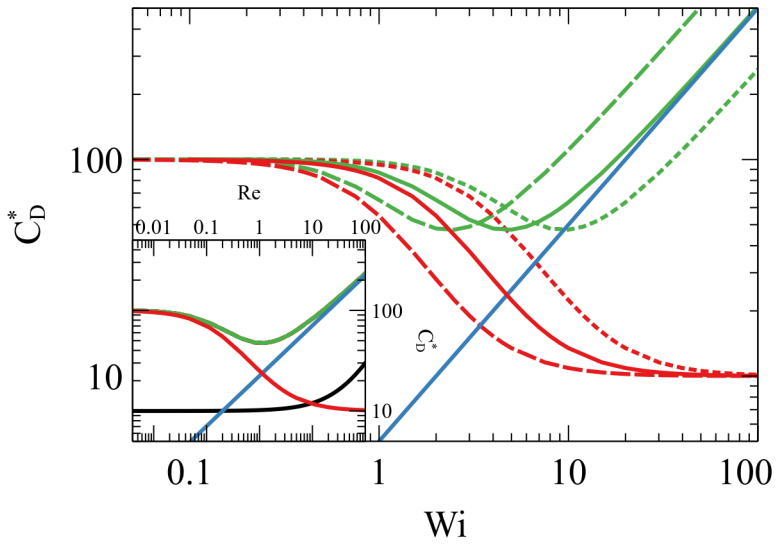

Figure 7: Total drag coefficient (green) with its viscous (red) and inertial (blue) contributions. The viscous contribution has been shifted along the x-axis by doubling (dotted) and halving (dashed) the polymer relaxation time τ_{p} in Eq. (22). The inset shows how all curves for the drag coefficient collapse when plotted as a function of the Reynolds number. Also included in the inset is the qualitative behavior of a Newtonian solvent (black solid line)

contributions in (19) and (20).

$$C_D^* = \frac{F_{\mathrm{I}} + F_{\mathrm{V}}}{R_{\mathrm{cyl}} v \eta_s} \tag{21}$$

In order to provide an analytical solution to equation 21, we need a rheological constitutive equation for the viscosity as a function of shear rate. To that end, we model the viscosity $\eta(\dot{\gamma})$ in Eq. (19) using the cross-model [59], which qualitatively resembles the viscosity curves in Figure 4:

$$\eta(\dot{\gamma}) = \eta_{\mathrm{s}} + \frac{\eta_0 - \eta_{\mathrm{s}}}{1 + (\tau_p \dot{\gamma})} \tag{22}$$

In Figure 7, we show the total drag coefficient and its contributions as predicted by Eqns. (19)–(22). This figure resembles quite well the simulation results with the onset of drag enhancement shifting to higher shear rates (or Wi numbers) as the characteristic polymer relaxation time τ_{p} increases. According to Eq. (21), the viscous contribution to the drag force will shift

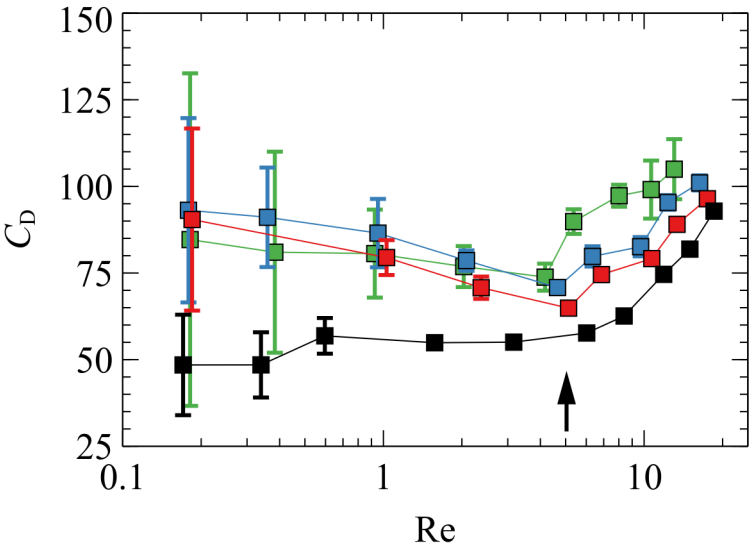

Figure 8: Drag coefficient as a function of the Re number. We use the same markers and color coding as in Figure 6. In addition we include the pure solvent results (black). The arrow shows the onset of drag enhancement at Re$\sim$ 5.

with the polymeric relaxation time while the inertial contribution will remain unaltered. This is demonstrated by the dashed and dotted lines in Fig. 7 for the viscous (red) and total (green) drag coefficient. We find further evidence of the drag enhancement being the result of inertia, if we look at C_{D}^{*} coefficient predictions as a function of the Re number. As shown in the inset to Fig. 7, all curves for different τ_{p} collapse into one. When we look at our simulation results in Figure 8, we observe that for the simulation data all curves also collapse into one suggesting that the increase in the drag coefficient is driven by inertia. The onset of drag enhancement appears at the same Reynolds number for all data sets (Re$\sim$ 5), including the pure solvent simulation results. For the solvent (no chains in the system), Newtonian behavior for C_{D} is observed with a progressive increase in the drag as inertia becomes dominant (See model prediction in the inset to Figure 7).

In addition to the analysis of the drag coefficients we have look at the velocity fields for the critical cases in the drag curves. Figure 9 shows the velocity magnitude ($v = \sqrt{v_x^2 + v_z^2}$) field for the minimum and maximum in the drag curves at Re=4.7 and Re=16.3 respectively. We observe a clear shift of the maximum magnitude of the velocity towards the outlet of the channel for the highest Re as a result of inertial effects. However, we do not observe

significant fluctuations in the magnitude of the velocity profiles. Haward *et al.* have reported the development of vertically asymmetric flow (i.e., by comparing to top and bottom halves of the domain) beyond a first critical Weissenberg number $\mathrm{Wi}_{c1} = 60$ and time dependent turbulent-like flow after a second critical Weissenberg number $\mathrm{Wi}_{c2} = 130$ [60]. In our simulations however, we only find horizontal asymmetry between the front and the back of the cylinders and the flow remains time independent up to Wi= 98. In their work, inertial effects are negligible and the blockage ratio ($2R/H = 0.1$) is much lower than in our simulations, where $2R/H = 0.5$. Simulation work on the symmetry and stability of flow around a single cylinder using the Phan-Thien-Tanner (PTT) model for viscoelasticity has also shown the critical Wi to increase with the ratio of the solvent to the total viscosity ratio $\beta = \eta_s/\eta$ [61] and the blockage ratio [62]. Similar qualitative behavior is observed with the inclusion of additional cylinders downstream in the channel [63]. As shown in Figure 4, at a concentration $w = 0.5$ we have $\beta \sim 0.5$. The absence of vertical asymmetry in our simulations can be explained by the high β (i.e., vertically asymmetric flow might develop at higher Wi numbers that were not accessible by our simulation).

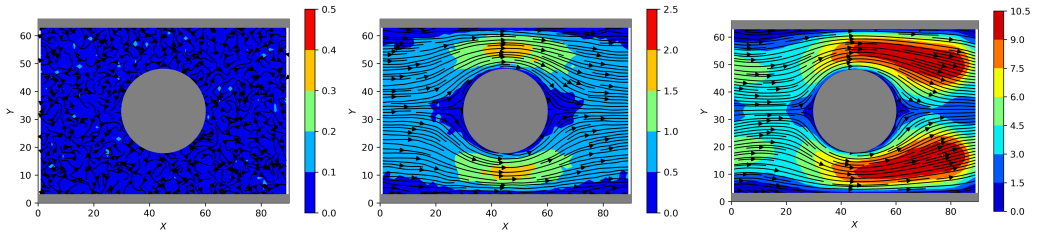

(a) (b) (c)

Figure 9: Analysis of the velocity field for $N = 50$ and $w = 0.5$: (a) Wi= 0.0 (Re= 0.0), (b) Wi= 28 (Re= 4.7) and (c) Wi= 98 (Re= 16.3). Streamlines are shown as black arrows. In the absence of flow (a), only small thermal fluctuations in the velocity are observed. (b) and (c) show the velocity field at the state with the minimum and maximum drag in Figure 8. Note the different colorbar scale for each figure.

3.2. Polymer migration

In addition to the inertia-driven drag enhancement, our simulations of the flow around an array of cylinders show chain migration throughout the range of Re (Wi) studied. Polymer migration has been shown to increase with Pe and Re in confined Poiseuille flow using Dissipative Particle Dynamics [64]. In our simulations, polymer chains migrate towards the center streamlines

(i.e., away from the channel walls) in the inlet/outlet regions. We also find a depleted area of near zero polymer concentration in the wake of the cylinder. The migration of chains is most significant at the stagnation point in the wake of the cylinder (see Figure 11). Note that no cavitation is found in this area since solvent particles are always present and the fluid density remains constant. However, the presence of migration and its magnitude does not simply follow either Re or Wi. We observe that the extend of migration is also dependent on the polymer's length N. Furthermore, we do not observe the creation of depletion zones [21] upstream of the cylinder, instead polymer concentration is increased around the cylinder front and the first half of the domain (See Figure 13f). Polymer (DNA molecules) migration – driven by the curvature of streamlines – has been observed in shear dominated flows in a cone-plate geometry by MacDonald *et al.* [20]. This study observed an increase in the concentration of chains close to 200% near the apex of the cone after long times under steady shear. To separate the effect of the possible mechanisms leading to migration in our simulations, we analyze the different regimes where depletion of chains are observed.

First, we look at the equilibrium distribution of chains in our simulation in the absence of flow in Figure 10 (a)-(c). We observe depletion near the channel and cylinder walls. The depleted areas are more apparent when we look at the density the center of mass of chains ρ_{c} in Figure 10 (d)-(f). As an additional indicator we look a the average chain conformation throughout the domain. We define the conformation tensor

$$\boldsymbol{c} = \frac{1}{N_{\mathrm{p}} q_0^2} \sum_{i}^{N_{\mathrm{p}}} \boldsymbol{q}_i \boldsymbol{q}_i \tag{23}$$

where N_{p} is the number of polymer chains in a given domain and $\boldsymbol{q}_i$ is the end-to-end vector of each chain in the domain. Figures 10 (g)-(i) shows the equilibrium trace of the conformation tensor for system with N=25, 50 and 100. Note that as expected, the average values are around $\mathrm{tr}(\boldsymbol{c}_{\mathrm{eq}})$=2, since we are representing a 2D projection in the xy-plane. However, the distribution of the trace becomes less homogeneous as N increases due to: (1) the relative small number of chains (i.e., from N=25 to N=100 we go from an average $\bar{N}_{\mathrm{p}} \sim 20$ to only 5), and (2) the exclusion near the wall and the cylinder that is discussed later as migration mechanism 1.

A detailed depiction of flow-induced migration of chains over the range in the dimensionless numbers space in this study is presented in Figure 11.

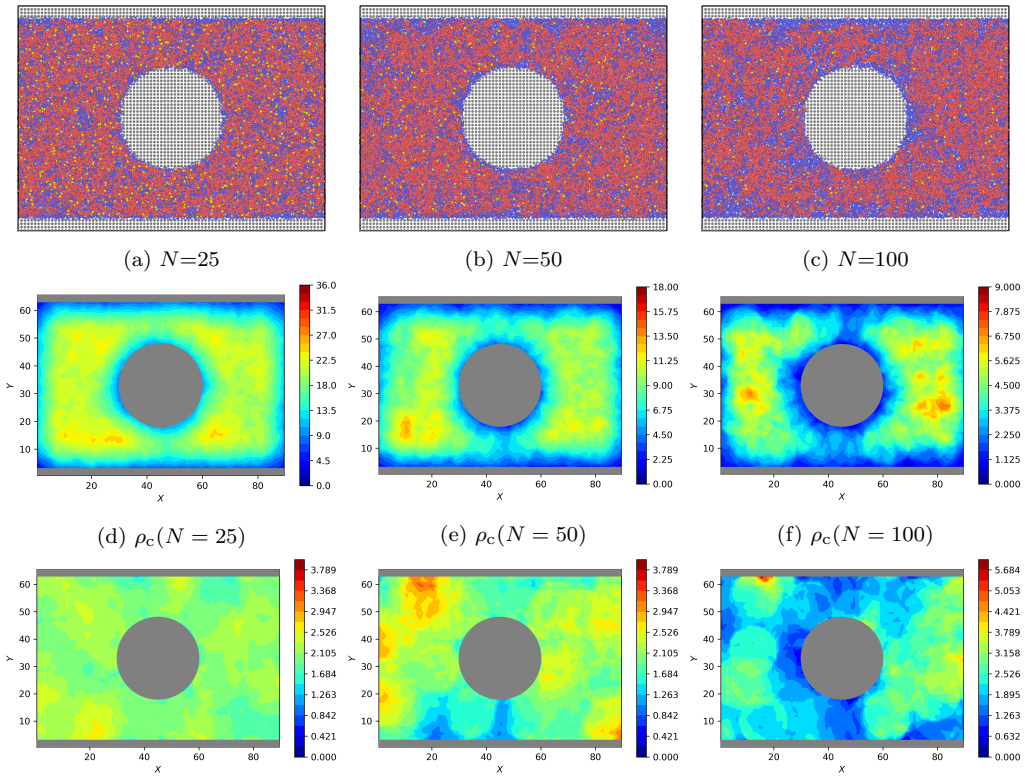

(a) N=25 (b) N=50 (c) N=100

(d) $\rho_c(N = 25)$ (e) $\rho_c(N = 50)$ (f) $\rho_c(N = 100)$

(g) $\mathrm{tr}(\boldsymbol{c})_{N=25}$ (h) $\mathrm{tr}(\boldsymbol{c})_{N=50}$ (i) $\mathrm{tr}(\boldsymbol{c})_{N=100}$

Figure 10: Equilibrium chain distribution around a cylinder for N=25 (a), N=50 (b) and N=100 (c) using the same color coding for the particles as in Fig. 5. For these three systems: (d)-(f) Show a 10 frame average of the number density of the center of mass of chains ρ_c for the same equilibrium configurations. In this plots wall exclusion of the order R_{g} increasing with N is observed. And (g)-(i) show a 10 frame average of the equilibrium trace of the conformation tensor $\boldsymbol{c}$.

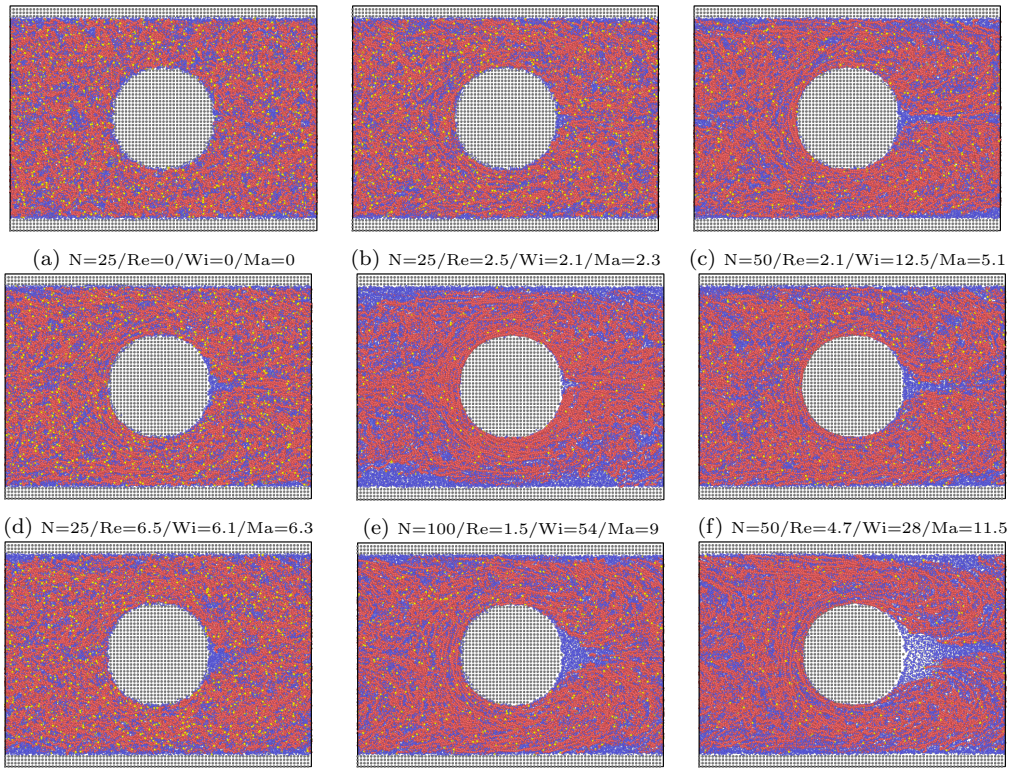

(a) N=25/Re=0/Wi=0/Ma=0 (b) N=25/Re=2.5/Wi=2.1/Ma=2.3 (c) N=50/Re=2.1/Wi=12.5/Ma=5.1

(d) N=25/Re=6.5/Wi=6.1/Ma=6.3 (e) N=100/Re=1.5/Wi=54/Ma=9 (f) N=50/Re=4.7/Wi=28/Ma=11.5

(g) N=25/Re=12.7/Wi=11.8/Ma=12.2 (h) N=50/Re=9.7/Wi=58/Ma=23.7 (i) N=100/Re=8.1/Wi=283/Ma=48

Figure 11: Chain distribution examples for flow around a cylinder for N=25, N=50, N=100. We have used the same color coding for the particles as in Fig. 5 and reduced the solvent particles display size to better visualize migration effects.

Notably, as we explore systems formed with chains of different length (although the concentration is kept constant w=0.5), we observe that Re and Wi numbers do not capture the onset or the extend of migration. For example in Figure 11f the Reynolds number (Re=4.7) is lower than in Figure 11d (Re=6.5), but we observe more migration in the former. The alternative case is shown in Figure 11f displaying more migration with Wi=28 than that of Figure 11e where Wi=54. This suggest that inertia or elasticity alone cannot explain the growth of the depleted areas. Instead, we observe that the extend of migration increases with the viscoelastic Ma= $\sqrt{\mathrm{ReWi}}$ from Ma=0 (a) to Ma=48 (i) in Figure 11. Note that Wi is strongly dependent on N through the polymer relaxation time τ_{p}. This strong dependence is what allows us to separate between inertial (Re) and elastic (Wi) effects. We conclude that neither Re nor Wi alone can predict the extent of migration in our system but rather a combination of the two through the viscoelastic Ma. We can rewrite the viscoelastic Mach number as Ma=$\sqrt{\tau_\nu \tau_{\mathrm{p}}}/\tau_{\mathrm{f}}$, where the relevant time scales in the flow are represented: the viscous time $\tau_\nu = R_{\mathrm{cyl}}^2/\nu$, the polymer relaxation time τ_{p}, and the flow characteristic time $\tau_{\mathrm{f}} = R_{\mathrm{cyl}}/\bar{v}$. In this way, Ma represents a balance between the geometric mean of viscous and polymeric relaxation times and the flow characteristic time given by the flow rate. Ma has been used to study the elastic waves induced by coil stretching at moderate Re and by streamline curvature at low Re in flow around cylinders [53, 12]. Furthermore Ma$\geq$1 has been correlated with downstream instabilities [22]. In our simulation we observe stable laminar flow (See Figure 9) with polymer migration throughout the range 1$\leq$Ma$\leq$48.

The transport of polymers in complex confined geometries is not fully understood [65]. We analyze our results in view of the migration mechanisms recently proposed by Jiang *et al.* in periodic contraction geometries [24]. First mechanism to consider is near-the-wall exclusion from layer with a size of the order of the equilibrium molecular size R_{g}. We observe this effect in regions of the upper and lower wall and surrounding the cylinder even in the initial equilibrium configurations. As shown by Figure 10, this effect is more pronounced as the polymer size increases (i.e., larger depleted regions are observed close to the walls and the cylinder in the absence of flow). For $N = 100$ in Figures 10 (c) and (f), the density of chains ρ_{c} on the top and bottom of the cylinder is strongly affected by this exclusion mechanism resulting in a non-homogeneous chain density field at equilibrium. This volume exclusion effect on the distribution of chains in the fluid domain can be explained by a transition from weak to moderate confinement as for N=100 the

$2R_g \sim 10$ becomes comparable to the gap between the cylinder and the wall [65]. Figures 10 (g), (h) and (i) show the trace of the conformation tensor averaged over 10 frames separated by 1000 timesteps each for N=25, 50 and 100 respectively. Note that near-the-wall exclusion affects the equilibrium distribution of the chain conformation tensor in Figure 10 (g)-(i) through the stretching of chains due to confinement but also through poor statistics in areas with low chain density leading to large fluctuations.

The second mechanism to consider is the sieving of chains through the contraction. This mechanism is only relevant when Wi< 1 [24] (i.e., polymer chains have not been significantly deformed). However at Wi<1, we do not observe a significant degree of migration beyond the depletion due to wall exclusion already present at equilibrium.

Next, we consider the kinetic theory for dilute polymer solutions given by Ma and Graham [66]. Using a spring dumbbell model the flux of polymer chains $\boldsymbol{j}$ is given by

$$\boldsymbol{j} = \rho_c \boldsymbol{v}_\infty - \boldsymbol{\nabla} \cdot (\rho_c \boldsymbol{D}_{K,\text{bulk}}) + \boldsymbol{M} : \boldsymbol{\tau} + \frac{\rho_c}{8} \boldsymbol{c} : \boldsymbol{\nabla}\boldsymbol{\nabla}\boldsymbol{v}_\infty \tag{24}$$

where ρ_c is the center of mass number density of chains, $\boldsymbol{v}_\infty$ is the bulk fluid velocity field, $\boldsymbol{M}$ the migration third order tensor[65], $\boldsymbol{\tau}$ the polymer stress tensor and $\boldsymbol{c}$ is the conformation tensor. Convection (first term) and diffusive transport (second term) can not produce an inhomogeneous polymer concentration field [66]. The third and fourth terms correspond with the third and fourth mechanisms described below respectively.

The third mechanism – migration of deformed chains due to HI with the walls – has been shown to be important in geometries with long contractions[25, 24]. The coupling between chain deformation and HI with the walls has been shown to drive polymers towards the center of straight channels [67, 68, 65, 64]. However, Jiang *et al.* showed that in a short periodic contraction geometry – close in length and blockage ratio to our array of cylinders – this mechanism is weak up to a Wi=30 [24].

Finally, we consider the two remaining mechanisms able to explain our results: Streamline-Curvature-Induced (SCI) and Depletion-Convection-Induced (DCI) migration. Both SCI and DCI mechanisms are characteristic of confined geometries and dependent on Wi. In our simulations the polymer size $R_g \sim 2-5$ and the radius of the cylinder $R_{cyl} = 15$. We highlight that for the polymer sizes and the geometry gap in our simulations the Gradient number Gd=$\sqrt{2/3}R_g/R_{cyl}$ varies from 0.1 to 0.2. This appears to be comparable to

the Gd=0.16 in Jiang *et al.*'s study in a contraction geometry.

In the fourth mechanism SCI, polymer chains traveling along curved streamlines migrate towards the center of curvature due to stress gradients. As indicated by the last term in Eq. 24, this mechanism is only relevant if the second derivative of the flow field is not negligible over the span of a polymer chain. SCI has been confirmed experimentally at Wi>1 [19, 20] and the rate of migration has been found to be proportional to Wi^2. As in the array of periodic square contractions in Jiang *et al.*'s study, our geometry presents a change of sign in the streamline curvature that could drive migration away from the stagnation point at the wake of the cylinder.

In contrast the fifth mechanism, DCI migration, results from the convective transport of a depleted layer near the wall in the contraction region (originally present due exclusion) towards the wider chamber [25]. In DCI, a gradient of velocity between layers with different polymer concentration creates a diffusion imbalance: chains traveling in faster flow layers lack the time to diffuse towards slower flow layers, while slower layers become more and more depleted in the wider slow areas. DCI has been applied in the separation of red blood cells from plasma in a constriction geometry [69]. As in Jiang *et al.*'s study, we take DCI to be characterized by a Peclét number $\mathrm{Pe}_{\mathrm{DCI}} = \frac{L_{\mathrm{d}}^2}{D_{\mathrm{p}}\tau_{\mathrm{DCI}}}$, where L_{d} is a characteristic depletion thickness layer and D_{p} is the center of mass diffusion coefficient of the polymer chain. The characteristic time is given by $\tau_{\mathrm{DCI}} = A/Q$, where Q is the flow rate per unit depth and $A = H(L_x/2 - R_{\mathrm{cyl}})$ is the area of the wide section of the channel behind the cylinder. We have seen that at equilibrium $L_{\mathrm{d}} \sim R_{\mathrm{g}}$ and for a Rouse chain we approximate $L_{\mathrm{d}}^2/D_{\mathrm{p}} \sim \pi^2\tau_{\mathrm{p}}$. DCI mechanism has been found to become dominant as the ratio between $\mathrm{Pe}_{\mathrm{DCI}}$ and Wi numbers increases [25, 24]. This ratio can be approximated as:

$$\frac{\mathrm{Pe}_{\mathrm{DCI}}}{\mathrm{Wi}} \simeq \frac{\pi^2}{3}\frac{R_{\mathrm{cyl}}^2}{A} \tag{25}$$

We find $\mathrm{Pe}_{\mathrm{DCI}}/\mathrm{Wi}$=0.4, which is twice the ratio in contraction geometry in Jiang *et al.* study ($\mathrm{Pe}_{\mathrm{DCI}}/\mathrm{Wi}$=0.2) [24], where SCI is established as the driving mechanism for migration. We highlight that for a slightly higher $\mathrm{Pe}_{\mathrm{DCI}}/\mathrm{Wi}$ ratio of 0.8 Ortiz *et al.* find DCI contributions to migration to be significant and it is possible that both mechanisms are contributing to the observed migration process. Qualitatively, it can be argued that a strong SCI migration will thin the depletion layer near the cylinder wall due to the

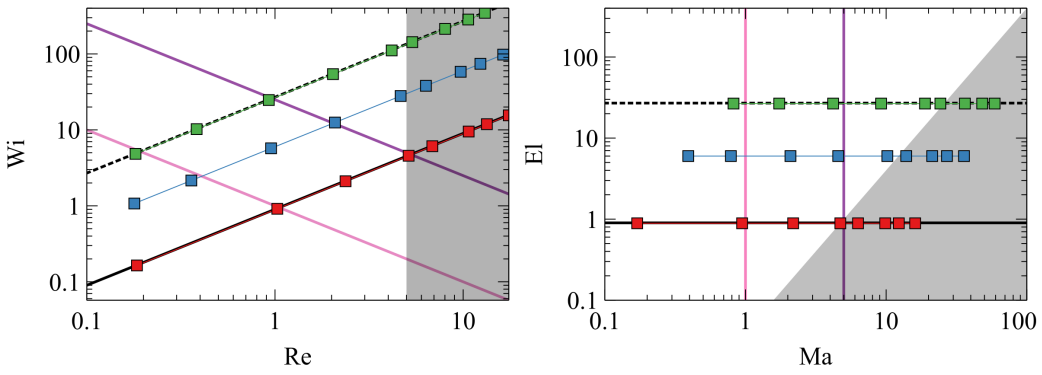

(a) (b)

Figure 12: Dimensionless parameter spaces for the simulations presented in this study: (a) Wi-Re and (b) El-Ma. Datasets with the same markers and color as in Figure 6. The black solid (dashed) line shows El=0.9 (El=27). The grey area shows Re$\geq$ 5 where drag enhancement is observed. The pink and purple solid lines represent Ma=1 and Ma=5 respectively. Migration is observed in all simulations with Ma>1 and its extend progresses with increasing Ma.

polymer alignment and stretching near the wall [24] (See Figures 11 and 13). This could potentially reduce the effect of DCI migration and, as a result, make SCI the dominant mechanism driving migration. The significant depletion at the wake of the cylinder agrees with description and characteristics of SCI due to the curvature of streamlines in that region. The modeling for SCI (also known as stress-gradient-induced) polymer migration in confined dilute solutions using continuum theory has been recently applied to Taylor-Couette flow [27] and flow between rotating eccentric cylinders [28]. These studies were limited to Wi$\leq$ 1.6 but already found migration towards the inner cylinder with near zero concentration at the outer cylinder wall. In our simulations, we also find migration toward the symmetry axis of the streamlines due to curvature as in [28]. However, we find the depletion at the wake of the cylinder correlates with the viscoelastic Ma and not the Wi if systems with different chain lengths (and polymer relaxation times) are studied. On the other hand, the moderate depletion near the walls in the wider flow regions could be attributed to DCI. Note that since migration is already significant for simulations below the critical Re=5, we can separate it from the inertia-induced drag increase discussed in the previous section.

In Figure 12, we look at the Wi-Re and El-Ma space covered in our simulations. The Elasticity number (El= Wi/Re = τ_p/τ_ν) considers the

polymeric relaxation time $\tau_{\rm p}$ and the viscous time $\tau_\nu = R_{\rm cyl}^2/\nu$. El has been used as an indicator for the transition between elastic, elasto-inertial and inertial regimes in polymeric solutions subjected to flow [1, 10]. In Figure 12a, we move on a line of constant El for each system with a fixed chain length by increasing the fluid's flow rate. We observe no correlation between drag enhancement and El. Instead drag enhancement triggered at Re$\geq$ 5 due to the fluid's inertia (grey area shown in Figure 12a), as the model presented in Section 3.1 suggests. Shi *et al.* presented a map for El-Ma to discriminate curvature driven instabilities in confined flows that resulted in non-homogeneous polymer concentration (i.e., migration). We have included that representation in Figure 12b. Both maps show the onset of polymer migration with a critical viscoelastic Mach number Ma=1 (pink solid lines in Figure 12). As discussed above, we find strong correlation between the extension of the polymer depleted area at the wake of the cylinder and Ma. We have included Ma=5 (purple) in both maps in Figure 12 to give an idea of how increasing the Ma number translates on each map. Note that Wi=Ma^2/Re and as a result, in Figure 12a for a fixed Ma number we have Wi to be inversely proportional to Re. The analysis of either of these maps shows a clear separation between the two phenomena encountered: drag enhancement and polymer migration. However, for sufficiently large Re both regions Ma>1 and Re>5 overlap.

In Figure 13 we show the density of chains for the velocity profiles in Figure 9. Note that the density of chains near the wall and on the wake of the cylinder goes down to zero in regions whose size increases roughly with Re, Wi and Ma numbers (i.e., once we fix the chain length N=50 the trends with these three dimensionless numbers are equivalent).

Figure 13 focuses on the system with N=50 at equilibrium (Re=0) and at the minimum (Re=4.7) and maximum (Re=16.3) in the drag curve in Figure 8. These states correspond with the same shown in Figure 9 for the velocity fields. For Re=0 in (a), we observe small fluctuations around the expected value tr($\boldsymbol{c}_{\rm eq}$)=2. For Re=4.7 in (b), we observe significantly larger values of the trace of $\boldsymbol{c}$ up to $\sim$12 with the most stretched chains found on top and below the cylinder. The asymmetry in the stretching (top to bottom) might be explained by the reduced chain density with slight differences between the top and the bottom of the cylinder (See Figure 13 (e)). As the flow rate is further increased (Re=16.3), the significant stretching above and below the cylinder in the contraction region shifts downstream and the most stretched chains are found in the wake of the cylinder. Note that in

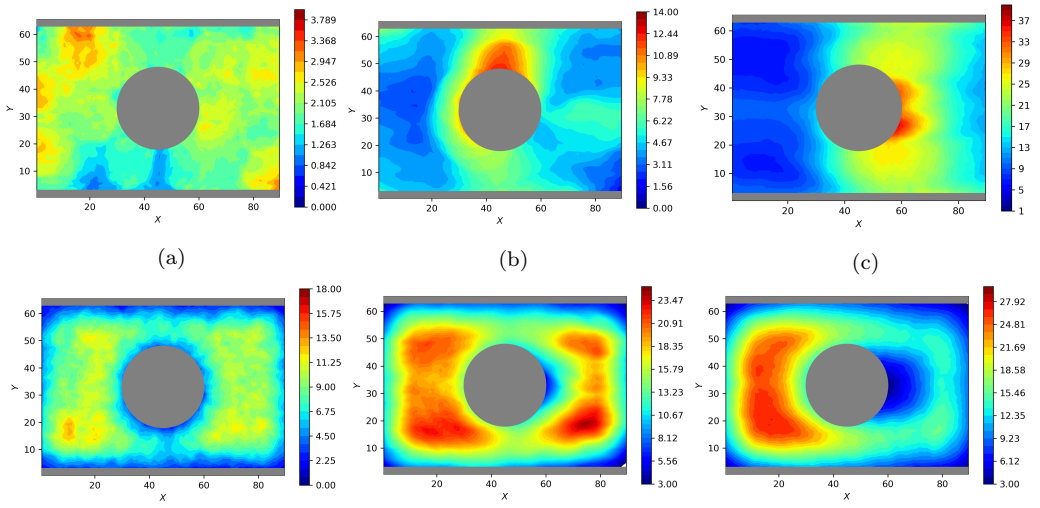

(a) (b) (c)

(d) (e) (f)

Figure 13: Trace of the conformation tensor tr($\boldsymbol{c}$) for $N = 50$ and $w = 0.5$ with Re=0.0 (Ma=0.0) (a), Re=4.7 (Ma=11.5) (b) and Re=16.3 (Ma=23.7) (c). The density of the center of mass of chains for flow around a cylinder for the same states are shown in (d), (e) and (f). The polymer depleted areas and asymmetry front to back increase progressively as the flow rate is increased. Trace and density panels result from the average over 10 frames separated by 1000 timesteps each.

this region very few chains are present (see Figure 13 (f)). Also noteworthy is the development strong asymmetry between the front and back of the cylinder while the top to bottom symmetry is recovered. This shift towards the back of the cylinder follows the velocity field in Figure 9 (c). In Figure 13 (b) and (c) we observe regions by the walls where chains are also more stretched. This effect is coupled with polymer migration and the reduced number of chains in these regions of the domain make it hard to draw strong conclusions. Note the velocity fields in Figure 9 do not show the effect of stretching or the top/bottom asymmetry observed for $\mathrm{tr}(\boldsymbol{c})$ in Figure 13 (b). An analysis of the stretching and recoiling of chains in this regime would be the subject of future work.

4. Conclusions

We have introduced a bottom-up mesoscopic model for viscoelastic polymeric solutions that mimics real fluid behavior. We present an exhaustive characterization of the of the static and dynamic properties of the fluid and validated the results with theoretical predictions based on the Zimm model. The rheological characterization of our model fluid subjected to Reverse Poiseuille flow shows a cross model behavior with shear thinning separated by two plateau regions. Finally, we simulate the flow around a confined array of periodic cylinders at moderate Re numbers. We find a small reduction in drag up to Re=5 and thereafter an inertia dominated regime with steep drag enhancement. To explain these results, we consider a simple model for the inertial and viscous contributions to the drag. Most experimental work on dilute solutions past obstacles, contraction flows or porous media have work in the inertia-less regime (very low Re) making direct comparison with our results impossible. We can compare our results for the drag to simulation work by Xiong *et al.* [18] at moderate values for Re and Wi using direct numerical simulations. They find Newtonian drag at low Re, drag enhancement at moderate Re. A drag reduction region at large Re is also found but we did not explore Re$>$ 20.

In our simulations, we also observe migration of polymer chains away from the channel walls and in the wake of the cylinder. We discuss five possible mechanisms contributing to migration and highlight Streamline-Curvature-Induced (SCI) and Depletion-Convection-Induced (DCI) migration as the main mechanisms driving the creation of polymer depleted areas in the flow. These two mecanisms are controlled by the ratio between the $\mathrm{Pe}_{\mathrm{DCI}}$ and the

Wi numbers. However, we find that the extent of the migration correlates well with the viscoelastic Mach number (Ma=$\sqrt{\mathrm{ReWi}}$) suggesting both elastic and inertial effects play a role in this phenomenon and that additional mechanisms might be needed to describe migration in confined geometries at moderate Re numbers. An analysis of the conformation of chains in these systems shows a coupling with the migration of chains and strong asymmetry between the from and the back of the cylinder.

Acknowledgements

This research is supported by the Basque Government through the BERC 2018-2021 program, by the Spanish State Research Agency through BCAM Severo Ochoa excellence accreditation SEV-2017-0718 and through the project PID2020-117080RB-C55 ("Microscopic foundations of soft-matter experiments: computational nano-hydrodynamics") funded by AEI - MICIN and acronym "Compu-Nano-Hydro".

References

[1] S. S. Datta, A. M. Ardekani, P. E. Arratia, A. N. Beris, I. Bischofberger, J. G. Eggers, J. E. López-Aguilar, S. M. Fielding, A. Frishman, M. D. Graham, J. S. Guasto, S. J. Haward, S. Hormozi, G. H. McKinley, R. J. Poole, A. Morozov, V. Shankar, E. S. G. Shaqfeh, A. Q. Shen, H. Stark, V. Steinberg, G. Subramanian, H. A. Stone, Perspectives on viscoelastic flow instabilities and elastic turbulence (2021). arXiv:2108.09841.

[2] A. Groisman, V. Steinberg, Elastic turbulence in a polymer solution flow, Nature 405 (6782) (2000) 53–55. doi:10.1038/35011019.
URL `https://doi.org/10.1038/35011019`

[3] J. Lawler, S. Muller, R. Brown, R. Armstrong, Laser doppler velocimetry measurements of velocity fields and transitions in viscoelastic fluids, Journal of Non-Newtonian Fluid Mechanics 20 (1986) 51–92. doi:https://doi.org/10.1016/0377-0257(86)80015-5.
URL `https://www.sciencedirect.com/science/article/pii/0377025786800155`

[4] M. A. Alves, R. J. Poole, Divergent flow in contractions, Journal of Non-Newtonian Fluid Mechanics 144 (2) (2007) 140–148. doi:https://doi.org/10.1016/j.jnnfm.2007.04.003.
URL `https://www.sciencedirect.com/science/article/pii/S0377025707000857`

[5] S. J. Haward, G. H. McKinley, Stagnation point flow of wormlike micellar solutions in a microfluidic cross-slot device: Effects of surfactant concentration and ionic environment, Phys. Rev. E 85 (2012) 031502. doi:10.1103/PhysRevE.85.031502.
URL https://link.aps.org/doi/10.1103/PhysRevE.85.031502

[6] M. Chilcott, J. Rallison, Creeping flow of dilute polymer solutions past cylinders and spheres, Journal of Non-Newtonian Fluid Mechanics 29 (1988) 381–432. doi:https://doi.org/10.1016/0377-0257(88)85062-6.
URL https://www.sciencedirect.com/science/article/pii/0377025788850626

[7] G. H. McKinley, R. C. Armstrong, R. Brown, The wake instability in viscoelastic flow past confined circular cylinders, Philosophical Transactions of the Royal Society of London. Series A: Physical and Engineering Sciences 344 (1671) (1993) 265–304. arXiv:https://royalsocietypublishing.org/doi/pdf/10.1098/rsta.1993.0091, doi:10.1098/rsta.1993.0091.
URL https://royalsocietypublishing.org/doi/abs/10.1098/rsta.1993.0091

[8] K. Arora, R. Sureshkumar, B. Khomami, Experimental investigation of purely elastic instabilities in periodic flows, Journal of Non-Newtonian Fluid Mechanics 108 (1) (2002) 209–226, numerical Methods Workshop S.I. doi:https://doi.org/10.1016/S0377-0257(02)00131-3.
URL https://www.sciencedirect.com/science/article/pii/S0377025702001313

[9] B. Qin, P. E. Arratia, Characterizing elastic turbulence in channel flows at low reynolds number, Phys. Rev. Fluids 2 (2017) 083302. doi:10.1103/PhysRevFluids.2.083302.
URL https://link.aps.org/doi/10.1103/PhysRevFluids.2.083302

[10] R. J. Poole, Three-dimensional viscoelastic instabilities in microchannels, Journal of Fluid Mechanics 870 (2019) 1–4. doi:10.1017/jfm.2019.260.

[11] P. Pakdel, G. H. McKinley, Elastic instability and curved streamlines, Phys. Rev. Lett. 77 (1996) 2459–2462. doi:10.1103/PhysRevLett.77.2459.
URL https://link.aps.org/doi/10.1103/PhysRevLett.77.2459

[12] L. Pan, A. Morozov, C. Wagner, P. E. Arratia, Nonlinear elastic instability in channel flows at low reynolds numbers, Phys. Rev. Lett. 110 (2013) 174502. doi:10.1103/PhysRevLett.110.174502.
URL https://link.aps.org/doi/10.1103/PhysRevLett.110.174502

[13] L. Rodd, J. Cooper-White, D. Boger, G. McKinley, Role of the elasticity number in the entry flow of dilute polymer solutions in micro-fabricated contraction geometries, Journal of Non-Newtonian Fluid Mechanics 143 (2) (2007) 170–191. doi:https://doi.org/10.1016/j.jnnfm.2007.02.006.
URL https://www.sciencedirect.com/science/article/pii/S0377025707000493

[14] D. Samanta, Y. Dubief, M. Holzner, C. Schäfer, A. N. Morozov, C. Wagner, B. Hof, Elasto-inertial turbulence, Proceedings of the National Academy of Sciences 110 (26) (2013) 10557–10562. arXiv:https://www.pnas.org/content/110/26/10557.full.pdf, doi:10.1073/pnas.1219666110.
URL https://www.pnas.org/content/110/26/10557

[15] P. C. Valente, C. B. da Silva, F. T. Pinho, Energy spectra in elasto-inertial turbulence, Physics of Fluids 28 (7) (2016) 075108. arXiv:https://aip.scitation.org/doi/pdf/10.1063/1.4955102, doi:10.1063/1.4955102.
URL https://aip.scitation.org/doi/abs/10.1063/1.4955102

[16] Y. Dubief, V. E. Terrapon, J. Soria, On the mechanism of elasto-inertial turbulence, Physics of fluids (Woodbury, N.Y. : 1994) 25 (11) (2013) 110817–110817. doi:10.1063/1.4820142.
URL https://doi.org/10.1063/1.4820142

[17] K. P. Nolan, A. Agarwal, S. Lei, R. Shields, Viscoelastic flow in an obstructed microchannel at high weissenberg number, Microfluidics and Nanofluidics 20 (7) (2016) 101. doi:10.1007/s10404-016-1765-7.
URL https://doi.org/10.1007/s10404-016-1765-7

[18] Y. L. Xiong, C. H. Bruneau, H. Kellay, Drag enhancement and drag reduction in viscoelastic fluid flow around a cylinder 91 (6) (2010) 64001. doi:10.1209/0295-5075/91/64001.
URL https://doi.org/10.1209/0295-5075/91/64001

[19] K. A. Dill, B. H. Zimm, A rheological separator for very large DNA molecules, Nucleic Acids Research 7 (3) (1979) 735–749. arXiv:https://academic.oup.com/nar/article-pdf/7/3/735/3843764/7-3-735.pdf, doi:10.1093/nar/7.3.735.
URL https://doi.org/10.1093/nar/7.3.735

[20] M. J. MacDonald, S. J. Muller, Experimental study of shear-induced migration of polymers in dilute solutions, Journal of Rheology 40 (2) (1996) 259–283. arXiv:https://doi.org/10.1122/1.550740, doi:10.1122/1.550740.
URL https://doi.org/10.1122/1.550740

[21] D. Kawale, G. Bouwman, S. Sachdev, P. L. J. Zitha, M. T. Kreutzer, W. R. Rossen, P. E. Boukany, Polymer conformation during flow in porous media, Soft Matter 13 (2017) 8745–8755. doi:10.1039/C7SM00817A.
URL http://dx.doi.org/10.1039/C7SM00817A

[22] X. Shi, S. Kenney, G. Chapagain, G. F. Christopher, Mechanisms of onset for moderate mach number instabilities of viscoelastic flows around confined cylinders, Rheologica Acta 54 (9) (2015) 805–815. doi:10.1007/s00397-015-0875-6.
URL https://doi.org/10.1007/s00397-015-0875-6

[23] X. Shi, G. F. Christopher, Growth of viscoelastic instabilities around linear cylinder arrays, Physics of Fluids 28 (12) (2016) 124102. arXiv:https://doi.org/10.1063/1.4968221, doi:10.1063/1.4968221.
URL https://doi.org/10.1063/1.4968221

[24] L. Jiang, R. G. Larson, Multiscale modeling of polymer flow-induced migration and size separation in a microfluidic contraction flow, Journal of Non-Newtonian Fluid Mechanics 211 (2014) 84–98. doi:https://doi.org/10.1016/j.jnnfm.2014.07.002.
URL https://www.sciencedirect.com/science/article/pii/S0377025714001104

[25] J. P. Hernadez-Ortiz, H. Ma, M. D. de Pablo, Juan J. adn Graham, Concentration distributions during flow of confined flowing polymer solutions at finite concentration: slit and grooved channel, Korean-Australia Rheology Journal 20 (3) (2008) 143–152.

[26] G. Zhu, H. Rezvantalab, E. Hajizadeh, X. Wang, R. G. Larson, Stress-gradient-induced polymer migration: Perturbation theory and comparisons to stochastic simulations, Journal of Rheology 60 (2) (2016) 327–343. arXiv:https://doi.org/10.1122/1.4942252, doi:10.1122/1.4942252.
URL https://doi.org/10.1122/1.4942252

[27] E. Hajizadeh, R. G. Larson, Stress-gradient-induced polymer migration in taylor–couette flow, Soft Matter 13 (2017) 5942–5949. doi:10.1039/C7SM00821J.
URL http://dx.doi.org/10.1039/C7SM00821J

[28] J. Xiang, E. Hajizadeh, R. G. Larson, D. Nelson, Predictions of polymer migration in a dilute solution between rotating eccentric cylinders, Journal of Rheology 65 (6) (2021) 1311–1325. arXiv:https://doi.org/10.1122/8.0000330, doi:10.1122/8.0000330.
URL https://doi.org/10.1122/8.0000330

[29] P. Español, M. Revenga, Smoothed dissipative particle dynamics, Physical Review E 67 (2) (2003) 026705.

[30] M. Ellero, P. Español, Everything you always wanted to know about sdpd (but were afraid to ask), Applied Mathematics and Mechanics 39 (1) (2018) 103–124. doi:10.1007/s10483-018-2255-6.
URL https://doi.org/10.1007/s10483-018-2255-6

[31] N. Moreno, M. Ellero, Arbitrary flow boundary conditions in smoothed dissipative particle dynamics: A generalized virtual rheometer, Physics of Fluids 33 (1) (2021) 012006. arXiv:https://doi.org/10.1063/5.0035936, doi:10.1063/5.0035936.
URL https://doi.org/10.1063/5.0035936

[32] R. H. Cole, Underwater explosions, Princeton University Press,, 1948.

[33] R. Courant, K. Friedrichs, H. Lewy, Über die partiellen differenzengleichungen der mathematischen physik, Mathematische Annalen 100 (1) (1928) 32–74. doi:10.1007/BF01448839.
URL https://doi.org/10.1007/BF01448839

[34] M. Ellero, P. Español, N. A. Adams, Implicit atomistic viscosities in smoothed particle hydrodynamics, Phys. Rev. E 82 (2010) 046702.

doi:10.1103/PhysRevE.82.046702.
URL https://link.aps.org/doi/10.1103/PhysRevE.82.046702

[35] R. Bird, R. Bird, R. Armstrong, O. Hassager, Dynamics of Polymeric Liquids, Volume 1: Fluid Mechanics, Dynamics of Polymeric Liquids, Wiley, 1987.
URL https://books.google.es/books?id=posvAQAAIAAJ

[36] S. Litvinov, Q. Xie, X. Hu, N. Adams, M. Ellero, Simulation of individual polymer chains and polymer solutions with smoothed dissipative particle dynamics, Fluids 1 (1) (2016) 7. doi:10.3390/fluids1010007.
URL http://dx.doi.org/10.3390/fluids1010007

[37] M. E. Fisher, Shape of a self-avoiding walk or polymer chain, The Journal of Chemical Physics 44 (2) (1966) 616–622. arXiv:https://doi.org/10.1063/1.1726734, doi:10.1063/1.1726734.
URL https://doi.org/10.1063/1.1726734

[38] V. Symeonidis, G. E. Karniadakis, B. Caswell, Schmidt number effects in dissipative particle dynamics simulation of polymers, The Journal of Chemical Physics 125 (18) (2006) 184902. arXiv:https://doi.org/10.1063/1.2360274, doi:10.1063/1.2360274.
URL https://doi.org/10.1063/1.2360274

[39] S. Litvinov, M. Ellero, X. Hu, N. A. Adams, Self-diffusion coefficient in smoothed dissipative particle dynamics, The Journal of Chemical Physics 130 (2) (2009) 021101. arXiv:https://doi.org/10.1063/1.3058437, doi:10.1063/1.3058437.
URL https://doi.org/10.1063/1.3058437

[40] N. Clisby, Accurate estimate of the critical exponent ν for self-avoiding walks via a fast implementation of the pivot algorithm, Phys. Rev. Lett. 104 (2010) 055702. doi:10.1103/PhysRevLett.104.055702.
URL https://link.aps.org/doi/10.1103/PhysRevLett.104.055702

[41] C. M. Schroeder, Single polymer dynamics for molecular rheology, Journal of Rheology 62 (1) (2018) 371–403. arXiv:https://doi.org/10.1122/1.5013246, doi:10.1122/1.5013246.
URL https://doi.org/10.1122/1.5013246

[42] P. de Gennes, Scaling Concepts in Polymer Physics, Cornell University Press, 1979.
URL https://books.google.es/books?id=Gh1TcAAACAAJ

[43] W. Jiang, J. Huang, Y. Wang, M. Laradji, Hydrodynamic interaction in polymer solutions simulated with dissipative particle dynamics, The Journal of Chemical Physics 126 (4) (2007) 044901. arXiv:https://doi.org/10.1063/1.2428307, doi:10.1063/1.2428307.
URL https://doi.org/10.1063/1.2428307

[44] J. H. Irving, J. G. Kirkwood, The statistical mechanical theory of transport processes. iv. the equations of hydrodynamics, The Journal of Chemical Physics 18 (6) (1950) 817–829. arXiv:https://doi.org/10.1063/1.1747782, doi:10.1063/1.1747782.
URL https://doi.org/10.1063/1.1747782

[45] A. P. Thompson, S. J. Plimpton, W. Mattson, General formulation of pressure and stress tensor for arbitrary many-body interaction potentials under periodic boundary conditions, The Journal of Chemical Physics 131 (15) (2009) 154107. arXiv:https://doi.org/10.1063/1.3245303, doi:10.1063/1.3245303.
URL https://doi.org/10.1063/1.3245303

[46] S. Plimpton, Fast parallel algorithms for short-range molecular dynamics, Journal of Computational Physics 117 (1) (1995) 1–19. doi:https://doi.org/10.1006/jcph.1995.1039.
URL https://www.sciencedirect.com/science/article/pii/S002199918571039X

[47] D. A. Fedosov, G. E. Karniadakis, B. Caswell, Steady shear rheometry of dissipative particle dynamics models of polymer fluids in reverse poiseuille flow, The Journal of chemical physics 132 (14) (2010) 144103–144103. doi:10.1063/1.3366658.
URL https://doi.org/10.1063/1.3366658

[48] J. A. Backer, C. P. Lowe, H. C. J. Hoefsloot, P. D. Iedema, Poiseuille flow to measure the viscosity of particle model fluids, The Journal of Chemical Physics 122 (15) (2005) 154503. arXiv:https://doi.org/10.1063/1.1883163, doi:10.1063/1.1883163.
URL https://doi.org/10.1063/1.1883163

[49] A. Savitzky, M. J. E. Golay, Smoothing and differentiation of data by simplified least squares procedures., Analytical Chemistry 36 (8) (1964) 1627–1639. doi:10.1021/ac60214a047.
URL https://doi.org/10.1021/ac60214a047

[50] J. Luo, K. Ying, J. Bai, Savitzky–golay smoothing and differentiation filter for even number data, Signal Processing 85 (7) (2005) 1429–1434. doi:https://doi.org/10.1016/j.sigpro.2005.02.002.
URL https://www.sciencedirect.com/science/article/pii/S0165168405000654

[51] M. Ellero, N. A. Adams, Sph simulations of flow around a periodic array of cylinders confined in a channel, International Journal for Numerical Methods in Engineering 86 (8) (2011) 1027–1040. doi:https://doi.org/10.1002/nme.3088.

[52] A. Vazquez-Quesada, M. Ellero, Sph simulations of a viscoelastic flow around a periodic array of cylinders confined in a channel: elastic instabilities,, Journal Non Newt. Fluid Mech 127 (2012).

[53] M. Grilli, A. Vázquez-Quesada, M. Ellero, Transition to turbulence and mixing in a viscoelastic fluid flowing inside a channel with a periodic array of cylindrical obstacles, Phys. Rev. Lett. 110 (2013) 174501. doi:10.1103/PhysRevLett.110.174501.
URL https://link.aps.org/doi/10.1103/PhysRevLett.110.174501

[54] J. G. Oldroyd, A. H. Wilson, On the formulation of rheological equations of state, Proceedings of the Royal Society of London. Series A. Mathematical and Physical Sciences 200 (1063) (1950) 523–541. arXiv:https://royalsocietypublishing.org/doi/pdf/10.1098/rspa.1950.0035, doi:10.1098/rspa.1950.0035.
URL https://royalsocietypublishing.org/doi/abs/10.1098/rspa.1950.0035

[55] A. Varshney, V. Steinberg, Elastic wake instabilities in a creeping flow between two obstacles, Phys. Rev. Fluids 2 (2017) 051301. doi:10.1103/PhysRevFluids.2.051301.
URL https://link.aps.org/doi/10.1103/PhysRevFluids.2.051301

[56] A. Varshney, V. Steinberg, Drag enhancement and drag reduction in viscoelastic flow, Phys. Rev. Fluids 3 (2018) 103302.

doi:10.1103/PhysRevFluids.3.103302.
URL https://link.aps.org/doi/10.1103/PhysRevFluids.3.103302

[57] S. Varchanis, J. Tsamopoulos, A. Shen, S. Haward, Reduced and increased flow resistance in shear-dominated flows of oldroyd-b fluids, Journal of Non-Newtonian Fluid Mechanics (11 2021).

[58] G. K. Batchelor, An Introduction to Fluid Dynamics, Cambridge Mathematical Library, Cambridge University Press, 2000. doi:10.1017/CBO9780511800955.

[59] M. M. Cross, Relation between viscoelasticity and shear-thinning behaviour in liquids, Rheologica Acta 18 (5) (1979) 609–614. doi:10.1007/BF01520357.
URL https://doi.org/10.1007/BF01520357

[60] S. J. Haward, N. Kitajima, K. Toda-Peters, T. Takahashi, A. Q. Shen, Flow of wormlike micellar solutions around microfluidic cylinders with high aspect ratio and low blockage ratio, Soft Matter 15 (2019) 1927–1941. doi:10.1039/C8SM02099J.
URL http://dx.doi.org/10.1039/C8SM02099J

[61] S. Varchanis, C. C. Hopkins, A. Q. Shen, J. Tsamopoulos, S. J. Haward, Asymmetric flows of complex fluids past confined cylinders: A comprehensive numerical study with experimental validation, Physics of Fluids 32 (5) (2020) 053103. arXiv:https://doi.org/10.1063/5.0008783, doi:10.1063/5.0008783.
URL https://doi.org/10.1063/5.0008783

[62] G. H. McKinley, P. Pakdel, A. Öztekin, Rheological and geometric scaling of purely elastic flow instabilities, Journal of Non-Newtonian Fluid Mechanics 67 (1996) 19–47, papers Presented at the Workshop on 'Unresolved Experimental Dilemmas in the Dynamics of Complex Fluids'. doi:https://doi.org/10.1016/S0377-0257(96)01453-X.
URL https://www.sciencedirect.com/science/article/pii/S037702579601453X

[63] C. C. Hopkins, S. J. Haward, A. Q. Shen, Purely elastic fluid–structure interactions in microfluidics: Implications for mucociliary flows, Small 16 (9) (2020) 1903872. arXiv:https://onlinelibrary.wiley.com/doi/pdf/10.1002/smll.201903872,

doi:https://doi.org/10.1002/smll.201903872.
URL https://onlinelibrary.wiley.com/doi/abs/10.1002/smll.201903872

[64] D. A. Fedosov, G. Em Karniadakis, B. Caswell, Dissipative particle dynamics simulation of depletion layer and polymer migration in micro- and nanochannels for dilute polymer solutions, The Journal of Chemical Physics 128 (14) (2008) 144903. arXiv:https://doi.org/10.1063/1.2897761, doi:10.1063/1.2897761.
URL https://doi.org/10.1063/1.2897761

[65] M. D. Graham, Fluid dynamics of dissolved polymer molecules in confined geometries, Annual Review of Fluid Mechanics 43 (1) (2011) 273–298. arXiv:https://doi.org/10.1146/annurev-fluid-121108-145523, doi:10.1146/annurev-fluid-121108-145523.
URL https://doi.org/10.1146/annurev-fluid-121108-145523

[66] H. Ma, M. D. Graham, Theory of shear-induced migration in dilute polymer solutions near solid boundaries, Physics of Fluids 17 (8) (2005) 083103. arXiv:https://doi.org/10.1063/1.2011367, doi:10.1063/1.2011367.
URL https://doi.org/10.1063/1.2011367

[67] R. M. Jendrejack, D. C. Schwartz, J. J. de Pablo, M. D. Graham, Shear-induced migration in flowing polymer solutions: Simulation of long-chain dna in microchannels, The Journal of Chemical Physics 120 (5) (2004) 2513–2529. arXiv:https://doi.org/10.1063/1.1637331, doi:10.1063/1.1637331.
URL https://doi.org/10.1063/1.1637331

[68] R. Kekre, J. E. Butler, A. J. C. Ladd, Comparison of lattice-boltzmann and brownian-dynamics simulations of polymer migration in confined flows, Phys. Rev. E 82 (2010) 011802. doi:10.1103/PhysRevE.82.011802.
URL https://link.aps.org/doi/10.1103/PhysRevE.82.011802

[69] M. Faivre, M. Abkarian, K. Bickraj, H. A. Stone, Geometrical focusing of cells in a microfluidic device: An approach to separate blood plasma, Biorheology 43 (2006) 147–159.